

1 **Enhancer-AAVs allow genetic access to oligodendrocytes and diverse populations of** 2 **astrocytes across species**

3
4 **Authors:** John K. Mich^{1*}, Smrithi Sunil², Nelson Johansen¹, Refugio A. Martinez¹, Mckaila Leytze¹,
5 Bryan B. Gore¹, Joseph T. Mahoney¹, Yoav Ben-Simon¹, Yemeserach Bishaw¹, Krissy Brouner¹,
6 Jazmin Campos¹, Ryan Canfield⁴, Tamara Casper¹, Nick Dee¹, Tom Egdorf¹, Amanda Gary¹, Shane
7 Gibson⁴, Jeff Goldy¹, Erin L. Groce¹, Daniel Hirschstein¹, Luke Loftus¹, Nick Lusk¹, Jocelin Malone¹,
8 Naomi X. Martin¹, Deja Monet¹, Victoria Omstead¹, Ximena Opitz-Araya¹, Aaron Oster¹, Christina A.
9 Pom¹, Lydia Potekhina¹, Melissa Reding¹, Christine Rimorin¹, Augustin Ruiz¹, Adriana E. Sedeño-
10 Cortés⁵, Nadiya V. Shapovalova¹, Michael Taormina¹, Naz Taskin¹, Michael Tieu¹, Nasmil J. Valera
11 Cuevas¹, Natalie Weed¹, Sharon Way¹, Zizhen Yao¹, Delissa A. McMillen¹, Michael Kunst¹, Medea
12 McGraw¹, Bargavi Thyagarajan¹, Jack Waters¹, Trygve E. Bakken¹, Shenqin Yao¹, Kimberly A. Smith¹,
13 Karel Svoboda², Kaspar Podgorski², Yoshiko Kojima^{3,6}, Greg D. Horwitz^{4,6}, Hongkui Zeng¹, Tanya L.
14 Daigle¹, Ed S. Lein^{1,7,8}, Bosiljka Tasic¹, Jonathan T. Ting^{1,4,6}, Boaz P. Levi^{1*}

15 16 **Author Affiliations:**

17 1 Allen Institute for Brain Science, Seattle WA, USA.
18 2 Allen Institute for Neural Dynamics, Seattle WA, USA.
19 3 Department of Otolaryngology Head and Neck Surgery, University of Washington, Seattle, WA, USA.
20 4 Department of Physiology and Biophysics, University of Washington, Seattle, WA, USA.
21 5 Division of Medical Genetics, University of Washington, Seattle, WA, USA.
22 6 Washington National Primate Research Center, University of Washington, Seattle, WA, USA.
23 7 Department of Neurological Surgery, Univ. of Washington, Seattle WA.
24 8 Department of Laboratory Medicine and Pathology, Univ. of Washington, Seattle WA
25 * Corresponding authors boazl@alleninstitute.org and johnmi@alleninstitute.org
26

27 **Abstract:** Proper brain function requires the assembly and function of diverse populations of neurons
28 and glia. Single cell gene expression studies have mostly focused on characterization of neuronal cell
29 diversity; however, recent studies have revealed substantial diversity of glial cells, particularly
30 astrocytes. To better understand glial cell types and their roles in neurobiology, we built a new suite of
31 adeno-associated viral (AAV)-based genetic tools to enable genetic access to astrocytes and
32 oligodendrocytes. These oligodendrocyte and astrocyte enhancer-AAVs are highly specific (usually >
33 95% cell type specificity) with variable expression levels, and our astrocyte enhancer-AAVs show
34 multiple distinct expression patterns reflecting the spatial distribution of astrocyte cell types. To provide
35 the best glial-specific functional tools, several enhancer-AAVs were: optimized for higher expression
36 levels, shown to be functional and specific in rat and macaque, shown to maintain specific activity in
37 epilepsy where traditional promoters changed activity, and used to drive functional transgenes in
38 astrocytes including Cre recombinase and acetylcholine-responsive sensor iAChSnFR. The astrocyte-
39 specific iAChSnFR revealed a clear reward-dependent acetylcholine response in astrocytes of the
40 nucleus accumbens during reinforcement learning. Together, this collection of glial enhancer-AAVs will
41 enable characterization of astrocyte and oligodendrocyte populations and their roles across species,
42 disease states, and behavioral epochs.

43 Introduction

44 Glial cell types play critical roles in CNS development, function, and homeostasis^{1,2}. Astrocytes provide
45 trophic support for neurons^{3,4}, coordinate regional wiring patterns⁵, respond to and regulate
46 neurotransmission^{6,7}, and drive repair or pathology after traumatic injury⁸⁻¹⁰. Oligodendrocytes form
47 myelin sheaths¹¹, strengthen circuits¹², secrete critical neurotrophic factors¹³, and contribute to
48 pathologic disease progression^{14,15}. Transcriptomic characterization of glial cells has revealed an array
49 of astrocyte and oligodendrocyte cell types, often with pronounced regional signatures¹⁸⁻²⁰.
50 Furthermore, species-specific features have been described²¹, although the functional significance of
51 these differences is unknown. Glial cell types have also been shown to play critical roles in CNS
52 diseases ranging from epilepsy²² to neurodegenerative diseases²³ to cancer^{24,25}. To understand how
53 glia differ between cell types, regions, species, and disease states, a set of tools is needed to grant
54 targeted genetic access to these specific populations across species.

55 Adeno-associated virus (AAV) vectors are exceptionally useful tools for somatic transgenesis across
56 mammalian species including human²⁶⁻³¹. Short enhancer or promoter regulatory elements work
57 effectively in AAV expression cassettes to drive cell-type selective gene expression in the brain or other
58 organs³²⁻³⁶. Recent work has shown that selective AAVs can be rationally designed by using enhancers
59 identified from epigenetic datasets that are selectively active and fit in an AAV vector³²⁻³⁶. Enhancer-
60 AAVs were recently developed to target different populations of excitatory and inhibitory neurons in the
61 brain, and some enhancers have shown successful targeting of glial cell populations as well^{37,38}.
62 However, the field largely relies on glial promoters that have some undesirable characteristics, most
63 notably loss of specificity or change in strength in different contexts as seen for astrocytic *GFAP*
64 promoter fragments³⁹⁻⁴¹. Furthermore, single cell genomics studies have revealed region-specific
65 astrocyte cell types for which no current tools are available¹⁸⁻²⁰.

66 Here we present a collection of enhancer-AAVs that selectively target astrocytes and oligodendrocytes.
67 Twenty-five astrocyte and 21 oligodendrocyte enhancer AAVs were identified from mouse and human
68 neocortical epigenetic data that produced reporter expression that was highly specific for the intended
69 populations, often labeling more than half of the intended cells in the area, and with a wide range of
70 expression strengths. Multiple astrocyte-targeting vectors exhibited distinct CNS region-specific
71 expression patterns, whereas oligodendrocyte-selective vectors generally drove expression throughout
72 the entire CNS. Several enhancer-AAVs maintained selective expression for astrocytes or
73 oligodendrocytes across rat and macaque. Lastly, several astrocyte tools were adapted to drive
74 expression of functional transgenes like Cre or the detection of neurotransmitters to reveal the role of
75 astrocytes in neurobiology. We used astrocyte-selective AAV expressing iAChSnFR⁴² to measure the
76 dynamics of acetylcholine in astrocytes of the nucleus accumbens during reinforcement learning. This
77 collection of tools opens up new opportunities for selective labeling and functional interrogation of glial
78 cell types across species and disease states, and could have translational applications via AAV-based
79 therapeutics⁴³⁻⁴⁵.

80 Results

81 *Generation of astrocyte- and oligodendrocyte-specific enhancer-AAVs.* We identified putative
82 enhancers specific for astrocytes and oligodendrocytes from single cell/single nucleus assay for

83 transposase-accessible chromatin (sc/snATAC-seq^{35,36}) and single nucleus methyl-cytosine sequencing
84 (snmC-seq) studies from neocortex⁴⁶⁻⁴⁹. Thousands of astrocyte- and oligodendrocyte-selective
85 scATAC-seq peaks were identified previously in both human middle temporal gyrus (MTG) and mouse
86 primary visual cortex (VISp), averaging approximately 300-600 bp in size (**Figure 1A**). Additional
87 ATAC-seq datasets confirmed these peaks^{50,51}. Generally, astrocyte and oligodendrocyte candidate
88 enhancers were accessible in non-neuronal cells but not in neuronal cells across the human
89 forebrain^{35,50} (**Extended Data Figure 1A-F**), and in the corresponding astrocyte or oligodendrocyte
90 subclasses across the mouse forebrain without strong cell type preferences⁵¹ (**Extended Data Figure**
91 **1G-J**).

92 We used three strategies to identify putative enhancers for testing: “high specificity”, “high strength”,
93 and “marker gene” (**Figure 1B-E**). The “high specificity” nomination criteria (gold square or star icons)
94 required enhancers and their orthologs to show accessibility specifically for both mouse and human
95 astrocytes or oligodendrocytes but not other cell types^{35,36}. In addition, we required that these putative
96 enhancers not be detected in demethylated genomic regions in both mouse and human neuron
97 populations⁴⁷. A small number of these “high specificity” enhancers also showed specific demethylation
98 in bulk human and mouse glial cells⁴⁶ (marked by gold star icons). “High strength” putative enhancers
99 were selected on the basis of strong astrocyte-specific peaks using only mouse scATAC-seq data³⁶,
100 with strength measured by accessibility read count within peaks. Finally, “marker gene” putative
101 enhancers showed specific and strong accessibility near known astrocyte- and oligodendrocyte-specific
102 marker genes.

103 We tested putative enhancer function in AAV vectors upstream of a minimal promoter driving the
104 reporter SYFP2 and evaluated expression throughout the mouse brain after systemic administration of
105 PHP.eB-serotyped AAVs. Enhancer-AAVs that showed anticipated reporter expression, were further
106 evaluated for specificity, completeness of expression, and cross-species activity (**Figure 1C** and
107 **Extended Data Table 1**). All three strategies were effective, with approximately half of the candidates
108 for both cell types yielding astrocyte or oligodendrocyte expression patterns during primary screening.
109 Moreover, expression of many of those enhancers was confirmed to be on-target by antibody staining
110 and/or scRNA-seq (**Figure 1F,G** and see below).

111 *A collection of astrocyte-specific enhancer-AAVs.* We screened 50 candidate astrocyte-specific
112 enhancer-AAVs, and 25 (50%) of them labeled astrocytes specifically with SYFP2 expression
113 (**Extended Data Figure 2**). Astrocyte-specific enhancer-AAVs showed a range of expression strengths
114 and patterns (**Figure 2A-I**) and vectors were categorized based on their labeling as: “Most of the CNS”,
115 “Regional”, “Scattered”, “Weak” and “Mixed specificities”. “Most of the CNS” astrocyte enhancer-AAVs,
116 including eHGT_380h and the human *GFAP* promoter (GfaABC1D⁵²), labeled cells with astrocyte
117 morphology in both brain and spinal cord (SpC, **Figure 2A-B, G-H**). Other examples in this category
118 include eHGT_387m, eHGT_390h, eHGT_390m, and the synthetic element ProB12³⁷ (**Extended Data**
119 **Figure 2**). “Regional” astrocyte enhancer-AAVs showed regionally restricted expression, such as
120 eHGT_385m that labeled astrocytes primarily in the telencephalon (**Figure 2C, I, Extended Data**
121 **Figure 2**). Other “Regional” enhancer-AAVs labeled astrocytes in subcortical domains but not in the
122 telencephalon, such as eHGT_381h and MGT_E160m (**Extended Data Figure 2**); while eHGT_375m
123 only labeled Bergmann glia, specialized astrocytes in the cerebellar cortex (CBX, **Figure 2D**).

124 Interestingly, enhancers MGT_E120m and MGT_E160m labeled astrocytes in nearly mutually exclusive
125 regions (**Extended Data Figure 3**). “Scattered” enhancer-AAVs labeled astrocytes strongly but
126 sparsely in most brain regions. These enhancer-AAVs include eHGT_374m (**Figure 2E**) and its
127 ortholog eHGT_374h (**Extended Data Figure 2**). Enhancer-AAVs labeled as “Weak” gave astrocyte-
128 specific patterns with low expression of SYFP (e.g., eHGT_373m and 386m, **Extended Data Figure 2**).
129 Last, we designated several enhancer-AAVs as “Mixed specificities” because they labeled astrocytes
130 and neurons. For example, MGT_E118m labels many astrocytes strongly and specifically within the
131 telencephalon, but also labels neurons strongly in non-telencephalic structures like midbrain (MB), deep
132 cerebellar nuclei (CBN), and globus pallidus, external segment (GPe) (**Figure 2F, Extended Data**
133 **Figure 2**).

134 We quantified the specificity of many of these astrocyte-specific enhancer-AAVs using multiple
135 independent techniques. First, we characterized SYFP2-expressing cells with immunohistochemistry
136 (IHC) for Sox9, a marker of astrocytes throughout the brain⁵³ (**Figure 2J-O**). Many of the astrocyte-
137 specific enhancer-AAV vectors show high specificity, which we define as >80% specificity for the target
138 cell population³⁵. Astrocyte-specific enhancer-AAVs are usually >95% specific, and often >99% specific
139 in VISp for Sox9-expressing astrocytes (**Figure 2P**). Second, we also observed high specificity when
140 we isolated single SYFP2+ cells by flow cytometry and profiled them by scRNA-seq (**Figure 2P**).
141 Additionally, we assessed completeness of astrocyte labeling using IHC, and we observed that vectors
142 scored as “Most of CNS” often label >50% of astrocytes in VISp, but “Weak” or “Scattered” vectors
143 labeled many fewer astrocytes (**Figure 2P**). “Regional” vectors showed differing completeness across
144 brain regions as expected (**Figure 2P**). Whole-brain serial two-photon tomography (STPT) of mouse
145 brain transduced with astrocyte-specific enhancer-AAVs demonstrated distinct astrocyte morphologies
146 in multiple brain regions (**Figure 2Q**). Thus, our collection of astrocyte-specific enhancer-AAVs are
147 diverse with regard to the density of labeled cells, expression strength, and regionalization.

148 *A collection of oligodendrocyte-specific enhancer-AAVs.* We screened 43 candidate oligodendrocyte
149 enhancers, of which 21 (49%) gave oligodendrocyte-specific expression patterns (**Extended Data**
150 **Figure 4**). Unlike the astrocyte collection, the oligodendrocyte enhancer-AAVs all produced similar
151 expression patterns throughout the gray matter and white matter tracts without any obvious regional
152 specificity (**Figure 3A-I**), consistent with the majority of oligodendrocytes in scRNA-seq profiling
153 studies²⁰. Oligodendrocyte-specific enhancer-AAV vectors ranged in expression from strong (for
154 example eHGT_410m, eHGT_641m, eHGT_395h, and eHGT_396h **Figure 3A-D**) to moderate (for
155 example eHGT_409h, **Figure 3E**, and the Myelin Basic Protein (MBP) promoter^{27,54}, **Extended Data**
156 **Figure 4**) to weak (for example eHGT_400h, **Figure 3F**). These vectors also labeled oligodendrocytes
157 throughout the spinal cord (**Figure 3G-I**). We confirmed molecular oligodendrocyte characteristics of
158 the vector-labeled cells by co-staining with CC1, a marker of oligodendrocytes⁵⁵, which showed most
159 vectors were highly specific across multiple brain regions (**Figure 3J-O**). Quantification by
160 immunohistochemistry and scRNA-seq on sorted SYFP2-expressing cells showed >99% specificity and
161 >45% completeness of labeling in VISp for multiple vectors (**Figure 3P**). STPT demonstrated
162 myelinating oligodendrocyte morphologies in multiple parts of mouse brain (**Figure 3Q**). This collection
163 of oligodendrocyte-specific enhancer-AAV vectors shows a diversity of expression strengths, but
164 appears to label a homogeneous population of oligodendrocytes.

165 *Transcriptomic identities of astrocytes and oligodendrocytes.* To investigate distinctions among
166 enhancer-AAV-transduced cells, we performed SMARTerV4 scRNA-seq on sorted SYFP2-expressing
167 cells. We characterized 2040 cells from 47 mice injected with 31 different enhancer-AAVs (1-2 mice per
168 enhancer-AAV). After removing low-quality single-cell transcriptomes and cells not expressing the
169 SYFP2 transcript, we focused our analysis on 1946 high-quality single cells. Astrocytes and
170 oligodendrocytes separated in the UMAP space, as did astrocytes sorted from the distinct brain regions
171 including VISp, midbrain/hindbrain (MB/HB), and CBX (**Figure 4A**). The molecular distinctions among
172 regional astrocyte populations agree with findings from recent whole-brain atlases²⁰. Indeed, mapping
173 to a whole-brain taxonomic atlas indicates that, with high confidence, VISp-profiled astrocytes are
174 predominantly mapped to the *Gja1*- and *Gfap*-expressing cluster “5112 Astro-TE NN_3”²⁰, whereas
175 MB/HB-profiled astrocytes marked by eHGT_381h and MGT_E160m mapped primarily to the *Gja1*-
176 and *Agt*-expressing cluster “5109 Astro-NT NN_2”²⁰. Likewise, the CBX-profiled Bergmann glia
177 astrocytes mapped primarily to cluster identity “5102 Bergmann NN” as expected (**Figure 4B-D**). In
178 contrast, labeled oligodendrocytes largely mapped to *Cldn11*- and *Mog*-expressing and most abundant
179 oligodendrocyte cluster “5158 MOL NN”²⁰ regardless of the enhancer used to label them (**Figure 4E**),
180 confirming that oligodendrocyte enhancer-AAVs label a largely homogeneous population of
181 oligodendrocytes.

182 To understand the molecular regulation of our astrocyte and oligodendrocyte-selective enhancer-AAVs,
183 we performed de novo motif detection on a collection of specific and strong astrocyte and
184 oligodendrocyte enhancers (n = 15 each) using MEME-CHIP⁵⁶. This analysis yielded one motif
185 occurring in the majority of enhancers in each set (**Figure 4F,G**). These motifs had strong enrichments
186 as measured by MEME-CHIP E-values less than 0.01, corresponding to the expected number of
187 equally sized motifs of same or greater log likelihood ratio occurring in a set of random sequences of
188 equal nucleotide content. We mapped these motifs against known transcription factor (TF) motif
189 databases^{57–59}, which revealed top matches to the Zic family consensus motifs for astrocytes (JASPAR
190 accession numbers MA0697.2, MA1628.1, and MA1629.1; average of these three shown) and the Sox
191 family motif for oligodendrocytes (JASPAR accession number MA0442.1 [Sox10 shown], and also
192 Uniprobe accession numbers UP00030.1 and UP00062.1; **Figure 4F,G**). These analyses suggest that
193 Zic and Sox family transcription factors might be key determinants of astrocyte versus oligodendrocyte
194 identity in the CNS^{60–63}. Moreover, Zic and Sox gene family members were differentially expressed
195 between the profiled astrocytes and oligodendrocytes (*Zic5* 32-fold mean difference, non-parametric
196 Wilcoxon rank-sum test $W = 577624$, $p < 1e-16$; *Sox10* 455-fold mean difference, non-parametric
197 Wilcoxon rank-sum test $W = 9838$, $p < 1e-16$; **Figure 4H**). These results suggest Zic5 and Sox10 play
198 key roles in determining specificity of these glial enhancer-AAVs.

199 *Regional expression correlates with astrocyte cell type distribution.* Using STPT imaging, we observed
200 astrocyte-specific enhancer-AAVs to have two distinct expression patterns within the basal ganglia
201 circuit. Several enhancer-AAVs showed elevated expression in astrocytes of the dorsolateral striatum
202 and depletion in the globus pallidus (GP; **Figure 4I-K**), and several other enhancer-AAVs drove
203 stronger transgene expression in astrocytes in the GP compared with those of the lateral striatum
204 (**Figure 4L-N, Extended Data Figure 3**). To determine if these enhancer-AAV expression patterns
205 correspond to transcriptomically-defined astrocyte cell types, we evaluated the spatial distributions of all

206 astrocyte cell types in the mouse whole brain taxonomy²⁰. Interestingly, two closely related astrocyte
207 cell types were strongly enriched in the dorsolateral striatum and cortex (“5112 Astro-TE NN_3” and
208 “5113 Astro-TE NN_3”), while another was strongly enriched in the GP (“5109 Astro-NT NN_2”),
209 demarcating the same boundaries observed with the collection of astrocyte enhancer-AAVs (**Figure**
210 **4O-R**).

211 *Measuring and optimizing enhancer strength.* In some cases, enhancer-AAV might not drive sufficient
212 levels of a transgene to functionally affect the target cell. We sought to boost the expression levels of
213 some enhancers by assembling concatemers of “core” sequences. These core sequences are
214 responsible for the selective expression patterns and are often found in the central third of the original
215 enhancer region identified by snATAC-seq³⁵ (that is, ~100-200 bp core from ~300-600 bp original
216 enhancer, **Figure 5A**). We observed that concatenation of the core can substantially increase
217 expression from the original enhancer, such as eHGT_387m concatenated to 3xCore1(387m) (**Figure**
218 **5B,C**), eHGT_390h concatenated to 3xCore2(390h) (**Figure 5D,E**), or eHGT_390m concatenated to
219 3xCore2(390m) (**Figure 5F,G**) while retaining similar expression patterns (**Figure 5H-J**) and cell type
220 specificity (**Figure 5K**). However, concatenation sometimes resulted in a less dramatic effect on
221 expression, (e.g., 3xCore(410m) and 3xCore(641m); **Extended Data Figure 4**).

222 We established single-cell measurements of reporter expression to compare enhancer strengths. We
223 found that single-cell reporter fluorescence by flow cytometry correlated with vector read counts from
224 scRNA-seq for both astrocytes and oligodendrocytes (astrocyte Pearson correlation coefficient = 0.63, t
225 = 3.97, df = 24, p < 0.001 by correlation t-test; oligodendrocyte Pearson correlation coefficient = 0.53, t
226 = 2.82, df = 20, p < 0.05 by correlation t-test; **Figure 5L,M, Extended Data Figure 5**). These
227 measurements revealed that several concatenated enhancer-AAVs, including 3xCore2(390m) and
228 3xCore2(390h), drove the strongest expression among the vectors we have tested (**Figure 5L**),
229 consistent with the microscopy results (**Figure 5B-J**). Conversely, MB/HB (eHGT_381h and
230 MGT_E160m) and Bergmann glia (eHGT_375m) astrocyte enhancers have among the weakest
231 expression levels we have tested (**Figure 5L**), likely a consequence of selecting cortical glial
232 enhancers.

233 *Predictability of enhancer-AAV expression across tissues and disease states.* Recent work suggests
234 that AAV-mediated transduction and high transgene expression in organs such as the liver and dorsal
235 root ganglia is associated with toxicity^{31,64}. We tested if we could predict off-target activity from
236 enhancer accessibility profiles in a human body-wide epigenetic dataset⁶⁵. Different astrocyte-specific
237 enhancers showed either moderate or low accessibility across many body organs (**Figure 6A**). We
238 assessed off-target transgene expression in liver after intravenous delivery since PHP.eB capsid
239 transduces the liver⁶⁶. We observed that astrocyte enhancers with moderate levels of accessibility in
240 liver (eHGT_381h, 371m, 371h, and 386m) expressed SYFP2 in many hepatocytes, whereas the
241 enhancers with negligible liver accessibility (eHGT_387m, 375m, 390h, and 390m) expressed SYFP2
242 in only few hepatocytes (**Figure 6B-C**). In contrast, the *GFAP* promoter drives expression in many
243 hepatocytes, and that is not predictable from any epigenetic or transcriptomic atlases. Finally, we find
244 one astrocyte enhancer (eHGT_380h) that is predicted to have negligible liver accessibility but
245 expresses SYFP2 in many hepatocytes (**Figure 6C**). Thus, the whole-body epigenetic dataset⁶⁵
246 predicts liver expression from astrocyte enhancer-AAV vectors for 89% (8/9) of vectors tested.

247 *GFAP* expression can change expression in the context of disease or injury⁹, and the synthetic *GFAP*
248 promoter can change specificity when delivering different transgenes³⁹⁻⁴¹, suggesting this might be a
249 poor tool for genetic access to astrocytes in disease. We compared *GFAP* promoter and one of our
250 best enhancer-AAVs (eHGT_390m) in Dravet syndrome model mice since they have strong epilepsy-
251 associated reactive astrogliosis⁶⁷. We injected SYFP2-expressing enhancer-AAVs into these mice prior
252 to the Dravet syndrome critical period of high susceptibility to seizures and mortality at P21 and
253 analyzed tissues at P42 (**Figure 6D**). Significant hippocampal gliosis was seen in *Scn1a*^{R613X/+} Dravet
254 syndrome model mice, revealed by elevated endogenous *GFAP* immunoreactivity in all hippocampal
255 layers (**Figure 6E**). Concomitant with this gliosis, the *GFAP* promoter-driven AAV reporter changed its
256 expression pattern. Normally, this promoter drives moderate levels of astrocyte-specific reporter
257 expression. However, in the Dravet mice experiencing epilepsy, expression strength in astrocytes was
258 considerably elevated, and ectopic expression was observed in many dentate gyrus granule cell
259 neurons (**Figure 6E**). In sharp contrast, the eHGT_390m enhancer-AAV vector maintains astrocyte
260 specificity at moderate levels despite the profound reactive gliosis in these diseased animals (**Figure**
261 **6E**). These results suggest that some enhancer-AAV vectors can provide astrocyte-specific expression
262 across body organs and across disease states, though this may not be true for all enhancers or disease
263 states.

264 *Astrocyte-specific AAV-Cre*. AAVs that can selectively drive Cre recombinases are valuable tools for
265 mouse genetics since the AAV can be delivered somatically for cell type-specific recombination of
266 floxed alleles. As a proof of principle, we used eHGT_390m to express a partially disabled R297T
267 mutant Cre recombinase in *Ai14* reporter mice^{68,69} (**Figure 7A-D**). This vector produced 99% astrocyte -
268 specific recombination in many parts of mouse brain, including medulla, midbrain, hippocampus, and
269 cortex. Despite the high astrocyte specificity in many brain regions, neurons were labeled in the
270 thalamus, pontine gray, and the cerebellum (**Extended Data Figure 2**). Thus, the astrocyte-specific
271 recombination observed in most of the brain will allow this tool to be used in combination with Cre
272 reporters to better understand the roles of astrocytes in brain biology, but other tools will be required for
273 drive astrocyte-selective Cre in certain brain regions.

274 *Cross-species genetic access to astrocytes and oligodendrocytes*. We tested whether several glial-
275 selective enhancer-AAV vectors could maintain specific expression across species. We first tested
276 conservation in neonatal rats after ICV administration (**Figure 7E**). We found that eHGT_641m- and
277 3xCore(410m)-driven AAV vectors labeled rat cortical oligodendrocytes with high specificity (91 and
278 71% specific, **Figure 7F,G**). We also observed that eHGT_387m and 390m labeled rat cortical
279 astrocytes with high specificity (96 and 87% specific, **Figure 7H,I**). In addition, an optimized
280 3xCore2(390m) vector containing 4X2C miRNA binding sites to prevent any unwanted expression in
281 excitatory neurons⁷⁰ expressed SYFP2 strongly and specifically throughout the rat forebrain (98%
282 specific, **Figure 7J,K**). Note that astrocyte labeling completeness and spread to caudal brain structures
283 could not be assessed since ICV administered virus resulted in uneven spread. We also tested some
284 other vectors in rat which appeared to lose specificity for astrocytes (data not shown). Thus, some but
285 not all vectors identified in our mouse screen maintained specificity in rats after ICV injection into
286 neonates.

287 We extended these cross-species tests to non-human primate (NHP), using multisite intraparenchymal
288 injections (**Figure 7L**). We administered eHGT_410m AAV vector into motor cortex and observed cell
289 morphologies of myelinating oligodendrocytes throughout the cortical column (**Figure 7M-N**).
290 Interestingly, we also observed SYFP2-expressing cells with a different morphology: one to three
291 processes that spiral around stretches of tubular structures approximately 15-20 microns in diameter
292 often running perpendicular to the cortical pial surface (**Figure 7O**). These tubular structures have not
293 yet been defined and were not observed in mouse or rat testing, but both morphological types of
294 SYFP2-expressing cells co-expressed the oligodendrocyte marker *SOX10* by mFISH with high
295 specificity (94%, **Figure 7P**).

296 We also injected the somatosensory cortex with the astrocyte-specific eHGT_390m AAV vector and
297 observed many SYFP2-expressing cells with astrocyte morphology throughout the cortical column
298 (**Figure 7Q**; note a small number of large layer 5 pyramidal neurons labeled as well, which we did not
299 observe in mouse testing). SYFP2-expressing astrocytes co-expressed GFAP either in parenchyma
300 (**Figure 7R**) or in apposition to a large blood vessel (**Figure 7S**), and some showed fibrous morphology
301 in white matter (**Extended Data Figure 6**). Enhancer-AAV-labeled astrocytes also expressed the
302 astrocyte-specific transcript *FGFR3* with high specificity (92%) and about half of the *FGFR3*+ gray
303 matter astrocytes were labeled through the whole cortical depth near the injection site (51%) (**Figure**
304 **7T**). These studies suggest that enhancer-AAV vectors provide specific and dependable genetic access
305 to astrocytes and oligodendrocytes across multiple species and reveal morphological glial features not
306 observed in the mouse.

307 *Astrocyte specific sensing of cholinergic signals in the nucleus accumbens during behavior.* We next
308 asked whether our vectors would drive sufficient expression to obtain functional signals in a cell-type
309 specific manner. We created a vector driving astrocyte-specific expression of the acetylcholine indicator
310 iAChSnFR⁴² (**Figure 8A,B**), to detect extracellular acetylcholine fluctuations in the nucleus accumbens
311 (NAc) in an awake and behaving animal using fiber photometry. After stereotaxic injection, we
312 implanted optical fibers above the injection site to perform fiber photometry. We trained mice to perform
313 a dynamic foraging reinforcement learning task while we recorded photometry signals to assess bulk
314 acetylcholine fluctuations in the NAc. In the task, water-restricted mice chose freely between two lick
315 ports for a water reward after an auditory cue. Reward probabilities of the two lick ports were changed
316 in a block-design manner, which resulted in both rewarded and unrewarded trials (**Figure 8C**). During
317 these trials, the astrocyte-specific iAChSnFR vector drove sufficient expression to observe fluorescence
318 intensity fluctuations (**Figure 8D**) which can be seen to differ during individual rewarded and
319 unrewarded licks (**Figure 8D**, bottom left). Both rewarded and unrewarded trials showed an increase in
320 fluorescent signal at the time of choice, followed by a deviation in signal depending on whether the trial
321 was rewarded (**Figure 8E**). Astrocyte acetylcholine signals decreased more in rewarded trials than in
322 unrewarded trials (**Figure 8E**). In summary, these results indicate that glial-selective enhancer-AAVs
323 can be applied to measure functional acetylcholine dynamics in the NAc.

324

325 Discussion

326 Flexible and dependable tools to target glial cell populations will be essential to understand their
327 diverse roles in brain biology. Here we report a collection of astrocyte- and oligodendrocyte-specific
328 enhancers that can be used in AAV vectors and applied across species. Most of these enhancer-AAVs
329 generated highly specific labeling of astrocytes or oligodendrocytes, and often substantial
330 completeness of labeling. Detailed characterization revealed the enhancers showed a range of
331 expression strengths, and the astrocyte enhancers frequently exhibited regional enrichment and
332 differences in labeling densities. We demonstrate that this enhancer-AAV toolset can be applied: 1)
333 across species in mouse, rat and monkey, 2) in epileptic mice where gliosis is occurring without losing
334 specificity, and 3) to deliver Cre selectively to many astrocyte populations, and 4) to measure circuit
335 dynamics with a neurotransmitter sensor *in vivo*. As a result, these glial enhancer-AAVs will be useful
336 for interrogating the roles of these glial cell types in health and disease.

337 *Lesson learned from screening.* Several lessons were learned through the process of screening for
338 astrocyte and oligodendrocyte enhancer-AAVs. First, multiple selection criteria can identify strong glial
339 enhancer-AAVs. Excellent functional enhancers were derived from genome-wide peak selection across
340 mouse and human datasets of distinct epigenetic modalities, peak selection from one mouse dataset
341 based on peak strength, or peak selection only near marker genes. Second, screening one enhancer-
342 AAV at a time can be efficient for the identification of useful enhancer-AAVs. Nearly half of the
343 candidate enhancers proved to be specific for the targeted type, and this created a large and diverse
344 library of new enhancer-AAVs that labeled astrocytes or oligodendrocytes in different ways. Third, while
345 enhancers were identified from neocortex at the subclass level, brain-wide patterns match well to whole
346 brain cell gene expression atlas patterns²⁰. Specifically, oligodendrocytes appear homogeneous across
347 the brain, while astrocytes show prominent regional enrichments and differences in cell density. Fourth,
348 body-wide specificity of enhancer-AAV expression can be predicted based on body-wide epigenetic
349 datasets⁶⁵. Thus, off-target expression can be predicted and limited during the enhancer selection
350 process, and enhancers can be identified that label different cell types throughout the body. These
351 attributes will make enhancer-AAVs a valuable tool for precision gene therapy where only the cell
352 population of interest is expressing the therapeutic transgene.

353 *Enhancer-AAVs show diverse expression patterns.* We tested a large collection of astrocyte-selective
354 enhancer-AAVs and saw a diversity of expression patterns. Some astrocyte enhancer-AAVs
355 predominantly labeled in telencephalic structures, some in MB/HB structures, and others showed
356 sparse “Scattered” but uniform expression. Within the forebrain, we also observed multiple enhancer-
357 AAVs that showed mutually exclusive enriched or depleted expression in dorsolateral striatum or the
358 globus pallidus. These regional differences were reflected by region-specific astrocyte transcriptomic
359 profiles in agreement with recent results²⁰. The GPe astrocytes express high levels of GABA uptake
360 gene *Slc6a11*^{18,71,72} while striatal and cortical, but not GPe astrocytes express high levels of glutamate
361 uptake gene *Slc1a2*^{18,72,73}. This suggests that the astrocytes help selectively maintain glutamate or
362 GABA tone depending on the brain structure and astrocyte cell type. The functional roles of astrocytes
363 in different brain regions will require additional experiments that our collection of enhancer-AAVs may
364 facilitate. Similarly, it is not yet clear what produces “Scattered” astrocyte reporter expression, and the
365 answer will await future experiments.

366 *Enhancer-AAVs can be optimized to improve vector function.* Achieving functional levels of transgene
367 expression is critical for applying enhancer-AAV tools to learn new biology and deliver gene therapies.
368 We show that two astrocyte enhancers could be optimized through generation of a triple concatenated
369 core to produce significantly higher levels of transgene expression without sacrificing astrocyte
370 specificity. One such optimized tool was used to detect acetylcholine activity in the NAc. The NAc has
371 been implicated in reward-related reinforcement learning and receives inputs from dopaminergic and
372 serotonergic neurons, in addition to local cholinergic signaling^{74–77}. We used enhancer-AAVs to deliver
373 the acetylcholine indicator iAChSnFR to astrocytes within the NAc, and measured dynamics with fiber
374 photometry. This experiment showed that our astrocyte enhancer 3xCore2(390m) maintained faithful
375 astrocyte specificity after direct injection into NAc and expressed sufficient iAChSnFR for sensing of
376 acetylcholine in live awake animals. It also showed that iAChSnFR expressed by astrocytes could
377 readily detect acetylcholine dynamics in NAc, and that astrocytes are a good cellular compartment for
378 the sensor.

379 Different optimization efforts enabled the generation of a functional Cre-AAV that was specific for
380 astrocytes in most parts of the brain. Cre recombinases can lose specificity when expressed from
381 enhancer-AAVs, possibly due to low-level expression of this potent enzyme³². We were able to
382 successfully generate an astrocyte-selective Cre AAV using an attenuated Cre recombinase with the
383 R297T mutation^{68,69}, in combination with the eHGT_390m enhancer. As a result we produced a highly
384 specific somatic astrocyte Cre, despite some neuronal off-target expression in thalamus, cerebellum,
385 and a small brainstem nucleus. Similar optimization could be applied to generate Cres for
386 oligodendrocytes or other cell populations. We anticipate further optimizations to boost expression and
387 reduce background will be critical to create ideal enhancer-AAV tools.

388 *Enhancers-AAVs can be identified that have conserved specificity from mouse to monkey.* Our data
389 demonstrate that some astrocyte and oligodendrocyte enhancer-AAVs are active and selective across
390 species from mouse through monkey. This property will allow these tools to be applied somatically in
391 multiple organisms besides mice. Testing enhancers in monkeys revealed interesting morphological
392 differences compared to mouse. Abundant mature oligodendrocytes with large dendritic arbors were
393 labeled in both mouse and primate tissues with eHGT_410m, but this enhancer-AAV also labeled
394 SOX10+ cells wrapping around radial tubes (presumably blood vessels) in primate but not mouse. Also,
395 the astrocyte enhancer eHGT_390m labeled abundant protoplasmic astrocytes in the gray matter in
396 mouse and monkey, but also labeled several large fibrous astrocytes that were not observed in our
397 mouse experiments. The ability to function across species and label cells that are not obviously
398 represented in mouse tissue, makes this collection of enhancer-AAVs a powerful toolset to better
399 understand new biology. It also makes a compelling case that some of these enhancer-AAVs could be
400 suitable for use in human gene therapy where astrocyte or oligodendrocyte expression selectivity is
401 required.

402 *Enhancer-AAVs can be identified that appear to be state-independent.* AAVs that drive expression
403 using promoters can cause gene expression changes in a state dependent fashion. We showed that
404 the GFAP promoter changed expression strength and specificity in the context of epilepsy-induced
405 gliosis using an *Scn1a* haploinsufficiency model. This is not surprising since the *GFAP* gene is known
406 to change in response to disease and injury^{8,9}. Enhancer-AAV eHGT-390m, on the other hand, did not

407 show a change of expression. This could be due to it being selected based on cell type identity, and
408 most properties of cell types have not been seen to change character dramatically in the context of
409 disease^{22,78,79}. Enhancers can also be selected that do not change activity during development, aging,
410 or disease, in a similar way to avoid selecting enhancers predicted to have activity in off-target tissues.
411 As epigenetic datasets expand to cover these axes of disease, development, and aging, it will be
412 feasible to select only putative enhancers with the desired activity profile.

413 *Conclusion.* We have characterized a large collection of enhancer-AAV vectors for targeting astrocytes
414 and oligodendrocytes. These vectors will provide researchers with the ability to mark and manipulate
415 these critical cell types in a variety of species, genetic backgrounds, ages, and disease contexts, and
416 could also enable delivery of therapeutics. Combined with other recently discovered AAV-based
417 tools^{27,28,33–36,66}, our glial-targeting toolbox will help to advance our understanding of the roles of glial
418 cell types in brain biology, make the complex cellular anatomy of the brain more experimentally
419 tractable, and advance the development of AAV-based therapeutics for human CNS disorders.

420

421 **Methods**

422 *Epigenetic analysis and enhancer nomination.* We identified candidate astrocyte- and oligodendrocyte-
423 specific enhancers from cortical epigenetic datasets. We used the following datasets: human middle
424 temporal gyrus snATAC-seq³⁵, mouse primary visual cortex scATAC-seq³⁶, human frontal cortex snmC-
425 seq⁴⁷, mouse frontal cortex snmC-seq⁴⁷, human frontal cortex bulk mC-seq⁴⁶, and mouse frontal cortex
426 bulk mC-seq⁴⁶. A single cell glial snmC-seq dataset^{48,49} became available only after initial identification
427 of most of the enhancers described in this study. From the single nucleus/cell ATAC-seq datasets, we
428 aggregated reads according to cell subclass as in the references, and then called peaks using Homer
429 findPeaks (<http://homer.ucsd.edu/homer/>) with the -region flag, yielding typically tens of thousands of
430 peaks per subclass, sized approximately 300-600 bp, as previously described³⁵. To find differentially
431 methylated regions (DMRs) we either used the published regions by Luo et al. 2017 in Extended Data
432 Tables 5 and 6⁴⁷, and aggregated by subclass and then to all neurons using bedtools merge
433 (<https://bedtools.readthedocs.io/en/latest/>). Alternatively for bulk non-neuronal DMRs we used methylpy
434 DMRfind with minimum differentially methylated sites set to 1 on the dataset of Lister 2013, as
435 previously described^{35,47}. To convert mouse and human peak or DMR regions to each other's genomic
436 coordinates for direct intersectional analysis, we used liftOver ([https://genome.ucsc.edu/cgi-
437 bin/hgLiftOver](https://genome.ucsc.edu/cgi-bin/hgLiftOver)) with minMatch parameter set to 0.6. All peak regions described in this manuscript
438 successfully liftOver from human to mouse, and vice-versa, except eHGT_733m which does not have
439 an obvious human ortholog via liftOver.

440 To automatically identify peaks and DMRs genome-wide that are astrocyte- or oligodendrocyte-specific
441 within each dataset, we used a series of bedtools intersectBed
442 (<https://bedtools.readthedocs.io/en/latest/>) operations to filter for regions that are only detected in
443 astrocytes or oligodendrocytes. For the “high specificity” criteria, we found peaks that were specifically
444 detected in both human and mouse cortical astrocytes/oligodendrocytes^{35,36}, but did not overlap DMRs
445 from either human or mouse neurons of any subclass⁴⁷, and these candidate enhancers are marked by
446 gold square icons in Figure 1. These criteria yielded a set of 87 candidate astrocyte-specific enhancers
447 and 112 candidate oligodendrocyte-specific enhancers, and the top 17 (Astrocyte) or 16
448 (Oligodendrocyte) candidate enhancers were chosen from this list as ranked by Homer findPeaks
449 score. Homer findPeaks score is a measure of peak significance relative to local background, not peak
450 strength. Additionally, a small number of these “high specificity” criteria candidate enhancers also
451 overlapped with DMRs from both human and mouse non-neuronal cells⁴⁶ (3 Astrocyte and 4
452 Oligodendrocyte), and these are marked by gold star icons in Figure 1 and Extended Data Figure 1.

453 For the “high strength” criteria we found peaks that were specifically detectable in cortical astrocytes,
454 using mouse scATAC-seq data only³⁶, and agnostic to detection in human and methylation datasets.
455 This analysis yielded 2119 (astrocyte) and 3940 (oligodendrocyte) candidate enhancers, which were
456 ranked by read counts within the region, and the top 7 candidate enhancers for astrocytes from this list
457 were chosen. This ranking led to nomination of peaks that are overall stronger and longer, and these
458 candidate enhancers are marked with a purple triangle in Figure 1B, but accessibility profiles were not
459 always conserved in human tissue, as shown in Extended Data Figure 1A,C.

460 Some candidate enhancers were identified manually in the vicinity of known astrocyte or
461 oligodendrocyte marker genes by visual inspection of ATAC-seq read pileups on UCSC browser
462 (marked as “M” for Marker genes in Figure 1B). Methylation data was not visualized in this manual
463 nomination process. Importantly we found that both automatic and manual approaches can identify
464 peaks with high strength and specificity, as shown in Figure 1D-E.

465 Additionally, enhancer MGT_E160m was initially identified as a candidate enhancer for pericytes in
466 cortex using the data of Graybuck et al.³⁶, but it was found in the course of this study to instead label
467 mid/hindbrain astrocytes.

468 To model enhancer screening results as a generalized linear model, we confined analysis to 50
469 screened enhancers where we observed a clear yes/no screening result for both itself and its cross-
470 species ortholog. These candidate enhancers were eHGT_371, 372, 373, 375, 377, 379, 380, 382,
471 383, 384, 388, 393, 394, 398, 399, 401, 406, 407, 408, 374, 376, 390, 395, 409, and 410, both the m
472 and h orthologs for each. For each of these genomic regions we calculated candidate enhancer
473 strength (read CPM within either astrocytes or oligodendrocytes), candidate enhancer specificity
474 (defined as the proportion of astrocyte or oligodendrocyte enhancer strength relative to the summed
475 strength in all populations, using the data of Mich et al. or Graybuck and Daigle et al.^{35,36}), candidate
476 enhancer length in base pairs, region-segmented PhyloP using the previous method³⁵, and tabulated
477 whether each candidate enhancer’s partner ortholog worked (binary yes [1] or no [0]). We fit a logistic
478 generalized linear model of testing results from these predictors using glm() in R with the following
479 command:

```
480 glm( Screen_result_01 ~ Length + PhyloP + Specificity + Strength_cpm +  
481 Ortholog_result_01, family=binomial(link='logit'), data = data)
```

482 The significance of each coefficient to predict the screening result was determined from the coefficients
483 of the model, using the data as provided in Extended Data Table 1. Although high peak specificity and
484 strength were important criteria for candidate enhancer identification, these metrics each had little
485 predictive power to explain success or failure of screening collection testing as evidenced by
486 coefficients of fit to a logistic linear model (Extended Data Table 1; strength z-value = 1.43, $p = 0.15$;
487 specificity [defined as proportional strength within target cell subclass] z-value = -1.20, $p = 0.23$), similar
488 to enhancer length (z-value = -0.13, $p = 0.89$), enhancer sequence conservation measured by PhyloP
489 (z-value = 0.87, $p = 0.38$), and the presence of a functional ortholog in testing (z-value = 1.77, $p =$
490 0.077), which suggests that there are additional undiscovered elements that determine successes
491 versus failures in AAV-based enhancer screening. Overall, the null deviance was 67.3 on 49 degrees of
492 freedom, and the residual deviance was 57.7 on 44 degrees of freedom, again indicating little power of
493 these features to predict the screening results.

494 *Cloning and packaging enhancer-AAVs.* With candidate enhancers chosen, we next found their
495 predicted DNA sequence from genomic reference sequence using Bioconductor package Bsgenome⁸⁰.
496 We extracted the sequence and padded 50 bp to each side of the enhancer to provide room for forward
497 and reverse primer binding sites that capture the entire enhancer. From these padded sequences, we
498 used automatic primer design in Geneious to identify primer pairs within the 50 bp pads to specifically
499 amplify each enhancer, and append a constant 5' homology arm to each enhancer for automatic

500 Gibson assembly into reporter-AAV plasmid. We amplified the regions from C57Bl/6 tail snip DNA or
501 from human male genomic DNA (Promega catalog # G1471) using FastPhusion 2x Master Mix
502 (Thermo Fisher catalog # F548L), and >90% of the PCR reactions were successful on the first try. In
503 some cases we redesigned primers to attempt a second amplification.

504 We cloned into reporter backbone CN1244 (Addgene plasmid #163493) using the sites MluI/SacI and
505 the 5' primer homology arms F: TTCCTGCGGCCGACGCGT and R:
506 GACTTTTATGCCAGCCCGAGCTC, using Infusion kit (Takara catalog # 638949). For some
507 enhancers we instead cloned into a next generation reporter vector backbone that includes a SYFP2-
508 P2A-3xFLAG-H2B reporter for detection of cytosolic SYFP2 and nuclear FLAG for simultaneous
509 expression analysis and snRNA-seq, using the same cut sites and homology arms (see Extended Data
510 Table 1). We transformed infusion reactions into Mix N' Go (Zymo Research catalog # T3001)
511 chemically competent Stb13 E. coli (Thermo Fisher catalog # C737303) and selected on 100 ug/mL
512 carbenicillin plates. We cultured individual clones at 32 C, verified them by Sanger sequencing,
513 maxiprepmed them with 100 ug/mL ampicillin, and saved them as frozen glycerol stocks at -80°C.

514 We used maxiprep DNA for packaging into PHP.eB AAV particles. For routine enhancer-AAV screening
515 by intravenous delivery in mouse we generated small-scale crude AAV preps by transfecting 15 ug
516 maxiprep enhancer-reporter DNA, 15 ug PHP.eB cap plasmid, and 30 ug pHelper plasmid into one 15-
517 cm dish of confluent HEK-293T cells using PEI-Max (Polysciences Inc. catalog # 24765-1). After
518 transfection the next day we changed the medium to 1% FBS, and after 5 days the cells and
519 supernatant were collected, freeze-thawed 3x to release AAV particles, treated with benzonase (1 uL)
520 for 1 hr to degrade free DNA, then clarified (3000g 10min) and then concentrated to approximately 150
521 uL by using an Amicon Ultra-15 centrifugal filter unit at 5000g for 30-60 min (NMWL 100 kDa, Sigma
522 #Z740210-24EA), yielding a titer of approximately 3-5 E13 vg/mL. For large-scale gradient preps for
523 intraparenchymal injection into NHP or mouse or ICV injection into rat, we transfected 10 15-cm plates
524 of cells, and also purified preps by iodixanol gradient centrifugation. We assessed viral titer for both
525 crude and gradient AAV preps by digital droplet PCR on a BioRad QX200 system. All vectors showing
526 specific expression patterns will be made available through Addgene.

527 *Optimizing enhancer strength through concatemerization.* For some native enhancers that showed
528 specific expression patterns, we sought to boost their expression levels through concatemerization. To
529 concatemerized, we segmented the enhancer (typically approximately 400-600 bp) into approximately
530 thirds with approximately 25 bp of overlaps at the junctions (each a candidate "core" of approximately
531 200 bp), then designed a tandem array of three cores in series (approximately 600 bp). These synthetic
532 tandem array sequences were gene synthesized by Azenta/GeneWiz PRIORITYGene synthesis
533 service with flanking MluI/SacI sites for restriction enzyme digestion and ligation into corresponding
534 sites in CN1244. We then packaged and tested concatemerized PHP.eB enhancer-AAVs as above.

535 *Mice and injections.* All mouse experimentation was approved by Allen Institute Institutional Animal
536 Care and Use Committee (IACUC) as part of protocol #2020-2002. In these studies, we purchased
537 C57Bl/6J mice from The Jackson Laboratory (Stock # 000664). For enhancer screening these C57Bl/6J
538 mice were injected with AAVs in the retro-orbital sinus at age P21 with 5E11 genome copies of
539 AAV/PHP.eB viral vectors with brief isoflurane anesthesia. For enhancer validation studies (IHC) mice

540 were injected the same way but between ages P42 to P56. Tissues from mice were harvested at 3 to 4
541 weeks post injection for analysis. We perfused animals with saline then 4%PFA, and harvested brains
542 or other tissues and post-fixed in 4%PFA overnight, before rinsing and cryoprotecting in 30% sucrose
543 solution before sectioning at 30 micron thickness on sliding microtome with a freezing stage. For
544 enhancer screening we counterstained with DAPI and propidium iodide and mounted in Vectashield
545 Vybrance, and imaged on either a Nikon Ti-Eclipse or Nikon Ti-Eclipse 2 epifluorescent microscope,
546 Olympus FV-3000 confocal microscope, or Leica Aperio slide scanner. In some experiments where
547 noted, we tested enhancer-AAVs after bilateral intracerebroventricular (ICV) injection at age P2 using
548 the technique of Kim et al.⁸¹ These ICV-injected pups were harvested for tissue analysis at age P21.
549 For whole brain imaging of expression pattern, we performed sequential blockface imaging of brains
550 using the TissueCyte 1000 serial two-photon tomography system⁸².

551 For testing in Dravet syndrome model mice, 129S1/SvImJ -*Scn1a*^{em1Dsf/J} mice (strain # 034129) were
552 purchased from Jackson Laboratories and bred to C57Bl/6J mice to create *Scn1a*^{R613X/+} pups on a F1
553 hybrid C57Bl/6J:129S1/SvImJ background, and these pups were injected retro-orbitally at P21 with
554 tissue analysis at P42. Additionally, we also tested enhancer-AAV vectors in *CMV-Cre;Scn1a*^{A1783V/+}
555 pups on C57Bl/6J background, which were generated from crossing B6(Cg)-*Scn1a*^{tm1.1Dsf/J} male mice
556 (The Jackson Laboratory, strain #:026133) with homozygous CMV-Cre female mice (*B6.C-Tg(CMV-*
557 *cre)1Cgn/J*, The Jackson Laboratory, strain # 006054).

558 *Mouse immunohistochemistry (IHC)*. For IHC and ISH, we transcardially perfused mice with ice-cold 25
559 mL HBSS (Thermo Fisher Scientific # 14175079) containing 0.25 mM EDTA (Thermo Fisher Scientific
560 # AM9260G), followed by 12 mL of ice-cold 4% paraformaldehyde in 1x PBS, freshly prepared from
561 16% PFA (Electron Microscopy Sciences #15710). We dissected brains and other tissues from
562 carcasses and post-fixed them at 4 degrees overnight, and the next morning we rinsed the tissues with
563 fresh PBS, and then transferred to 30% sucrose solution in PBS for cryoprotection. For sectioning on
564 Leica CM3050 cryostat, we then embedded tissues in OCT cryo-compound (Tissue-Tek # 4583) at
565 room temperature at least 3 hours, then froze the blocks on dry ice and stored at -80°C until sectioning
566 at 25 micron thickness. Alternatively, we sectioned half-brains at 25 µm thickness on frozen 30%
567 sucrose solution slabs on a sliding microtome (Leica SM2000R) equipped with freezing stage. Sections
568 were stored at 4 degrees in PBS containing 0.1% sodium azide until analysis.

569 For IHC we used the following antibodies: chicken anti-GFP (Aves # GFP-1010), rabbit anti-Sox9 (Cell
570 Signaling clone D8G8H, # 82630S), mouse CC1 antibody (Abcam # ab16794), mouse anti-GFAP
571 (Millipore Sigma clone G-A-5, # G3893), with 5% normal goat serum (Thermo Fisher Scientific #
572 31872) and 0.1% Triton X-100 (VWR 97062-208) for blocking and permeabilization, and appropriate
573 Alexa Fluor-conjugated secondary antibodies for detection.

574 *Flow cytometry and single cell transcriptomics*. We prepared cell suspensions for flow cytometry and
575 single cell RNA-seq from brain tissue as previously described⁸³. Briefly, for flow cytometry, we perfused
576 mice transcardially under anesthesia with ACSF.1. We harvested the brains, embedded in 2% agarose
577 in PBS, then sliced thick 350 micron sections using a compresstome with blockface imaging, then
578 picked the sections containing the region of interest (VISp, or mid- and hindbrain, or cerebellar cortex),
579 and dissected out the regions of interest. We then treated dissected tissues with 30U/mL papain

580 (Worthington LK003176) in ACSF.1 containing 30% trehalose (ACSF.1T) in a dry oven at 35°C for 30
581 minutes. After papain treatment we quenched digestion with ACSF.1T containing 0.2% BSA, triturated
582 sequentially using fire-polished glass pipettes with 600, 300, and 150 micron bores, filtered the
583 released cell suspensions into ACSF.1T containing 1% BSA, centrifuged cells at 100g for 10 min, then
584 resuspended cells in ACSF.1T containing 0.2% BSA and 1 µg/mL DAPI prior to flow cytometry and
585 sorting on a FACSAria III (Becton-Dickinson). SYFP2 reporter brightness was measured as the ratio of
586 positive cell population mean fluorescence intensity, divided by the low mean fluorescence intensity of
587 autofluorescence in non-expressing cells. This measure of reporter brightness is more consistent than
588 positive cell population mean fluorescence intensity alone, due to differences in raw signal across days,
589 cytometers, and cytometer settings.

590 For single cell RNA-seq, we sorted single SYFP2+ cells into tubes and processed them via SMARTer
591 v4 using the workflow described previously⁸³, on 47 enhancer-AAV-injected mice. In each experiment
592 from one mouse injected with one single enhancer-AAV we sorted and profiled up to 48 cells per
593 experiment, and each measurement was taken from a distinct individual cell. After retroorbital
594 injections, enhancer-AAV SYFP2-expressing cells consisted of on average 7% of the positive brain
595 cells (range 0.1-20.1% of cells, n = 47 experiments). We sequenced single cell-derived SMARTer
596 libraries at 659996 ± 199038 (mean ± standard deviation) reads per library on an Illumina NovaSeq
597 instrument at Broad Institute (Cambridge, MA) or on an Illumina NextSeq instrument at Allen Institute
598 (Seattle, WA). We aligned the libraries to mm10 genome using STAR
599 (<https://github.com/alexdobin/STAR>), and also aligned them to the synthetic AAV transgene reference
600 construct using bowtie2 (<https://bowtie-bio.sourceforge.net/bowtie2/index.shtml>). From 2040 initial cells,
601 we excluded from analysis the libraries with poor library quality metrics, consisting of: firstly low-quantity
602 or degraded libraries (judged as less than 65% percentage of cDNA library sized greater than 400 bp,
603 consisting of 71 [3.4%] libraries in this study), and secondly those that lacked AAV transgene-mapping
604 reads (likely mis-sorted events, 23 [1.1%] of remaining libraries). Applying these filtering criteria yielded
605 a dataset for analysis of 1946 high-quality AAV transgene-expressing cells, with alignment rates of 92 ±
606 3% to mm10 genome and 4654 ± 1285 genes detected per cell (mean ± standard deviation). To assess
607 enhancer specificity within the cortex we mapped the high quality transgene-expressing SMARTer cells
608 to the SMARTer-based VISp cellular taxonomy generated by Tasic et al. using bootstrapped
609 hierarchical approximate nearest neighbor mapping^{20,83}, and quantified the specificity as the percentage
610 of positively sorted cells that mapped to the expected cell subclass (astrocytes or oligodendrocytes). To
611 test for significance of correlation of brightness by flow cytometry with expression levels by scRNA-seq,
612 we calculated Pearson's product-moment correlation coefficient by `cor.test()` function in R.

613 To understand different characteristics of different regional astrocyte populations we utilized
614 `scrattch.mapping` (<https://github.com/AllenInstitute/scrattch>) from the Allen Institute. To accomplish this
615 we first transformed these cells by principal component analysis and performed UMAP dimensionality
616 reduction on the first 40 principal components for visualization using the default scanpy parameters,
617 which clearly separated oligodendrocytes and regional groupings of astrocytes. For clustering
618 astrocytes we subset the dataset to astrocytes only, then identified the top 2000 genes ranked by
619 variance among them, recomputed UMAP projections from these high-variance genes, then performed
620 Leiden clustering⁸⁴ which identified VISp, MB/HB, and CBX astrocyte clusters as expected, and finally

621 identified differential genes among them (differential gene expression threshold false discovery rate
622 less than 5% and log₂-fold change greater than 0.5) using scanpy
623 (<https://scanpy.readthedocs.io/en/stable/>). In doing so we detected two major subgroups of VISp
624 astrocytes that are distinguished by presence or absence of immediate-early gene markers (for
625 example, *Fos*, *Fosl2*, *Nr4a1*, *Irs2*, *Pde10a*, and *Pde7b*). This distinction may be an artifact of our cell
626 dissociation process for scRNA-seq; for the purposes of this study we collapse these cortical astrocyte
627 clusters. In order to understand the different regional characteristics of astrocyte populations we
628 mapped cells to whole brain taxonomy we mapped to the best-correlated mean-aggregated taxonomic
629 cluster²⁰ with 100 bootstrapped iterations using the top 10% of high-variance genes and omitting a
630 variable number of genes (10-50%) each round. We interpret the frequency of correct mapping rounds
631 as the mapping confidence. We also used CELLxGENE for single cell visualization
632 (<https://github.com/chanzuckerberg/cellxgene>). Spatial transcriptomic analysis was performed as
633 described in the recent whole brain transcriptomic taxonomy study²⁰, and cell type location data was
634 visualized using CirroCumulus (<https://cirroCumulus.readthedocs.io/en/latest/index.html>).

635 For determination of *Zic5* and *Sox10* differential gene expression between astrocytes and
636 oligodendrocytes, we used two-sided ANOVA on expression measurements from individually profiled
637 cells from all the experiments with no exclusion, and no covariates were tested. Testing for normality by
638 the Shapiro-Wilk test revealed that *Zic5* and *Sox10* expression are not normally distributed (*Zic5* W =
639 0.539, p-value < 2.2e-16; *Sox10* W = 0.958, p-value = 5.1e-16), so we used a non-parametric Wilcoxon
640 rank-sum test. No significance thresholds adjustments were made for multiple comparisons since only
641 one comparison was performed. For the comparison of *Sox10* versus *Zic5* expression (mean counts
642 per million +/- standard deviation, n cells): astrocyte *Zic5* expression 32 ± 71, n = 864; astrocyte *Sox10*
643 expression 0.3 ± 5, n = 864; oligodendrocyte *Zic5* expression 0.6 ± 6, n = 964, oligodendrocyte *Sox10*
644 expression 456 ± 276, n = 964.

645 **Motif analysis.** We performed de novo motif discovery from the sets of astrocyte and oligodendrocyte
646 enhancers that showed specific and strong expression patterns, excluding those enhancers scored as
647 weak. For astrocytes this list consisted of: eHGT_375m, eHGT_376h, eHGT_376m, eHGT_377m,
648 eHGT_380h, eHGT_381h, eHGT_385h, eHGT_385m, eHGT_380h, eHGT_390h, eHGT_390m,
649 MGT_E120m, MGT_E122m, MGT_E160m, and ProB12. For oligodendrocytes this list consisted of:
650 eHGT_361h, eHGT_395h, eHGT_395m, eHGT_396h, eHGT_397m, eHGT_398h, eHGT_400m,
651 eHGT_401h, eHGT_403h, eHGT_407h, eHGT_409h, eHGT_409m, eHGT_410h, eHGT_410m, and
652 eHGT_641m. We used MEME-CHIP⁵⁶ to identify recurrent de novo motifs in these sets of sequences,
653 using the parameter -meme-maxw 12, and comparing to a background set of random sequence with
654 the same nucleotide content. This analysis revealed one strong motif in each set of sequences, as
655 measured by its E-value, which is an estimate of the number of motifs expected by chance to have as
656 strong a log likelihood ratio as itself within the given sequences. These de novo motifs were then
657 mapped to known sequences using TomTom⁵⁶ which revealed several possible matches to known
658 motifs at significant p-values, but the strongest motif match (lowest p-value) in each case is shown. In
659 the case of the *Zic* family transcription factors, for simplicity we averaged together the highly correlated
660 strongest hits in the *Zic* family (JASPAR accession numbers MA0697.2, MA1628.1, and MA1629.1
661 covering *Zic1*, *Zic2*, and *Zic3*), since *Zic5* itself is not present in databases. In the case of *Sox10*, the

662 highly correlated Sox family members Sox4 and Sox11 (Uniprobe accession numbers UP00062.1 and
663 UP00030.1) showed slightly stronger motif match p-values than Sox10 (JASPAR accession number
664 MA0442.1), but these were excluded from analysis due to lack of expression in almost all
665 oligodendrocytes as observed by Tasic et al.⁸³ and in this study.

666 *Enhancer-AAV testing in rat.* The Allen Institute Institutional Animal Care and Use Committee (IACUC)
667 approved the following in vivo testing experiments in rat under protocol 2010. We procured timed-
668 pregnant female Sprague-Dawley rats from Charles River laboratories. We tattooed and injected ice-
669 anesthetized neonatal pups at P1 with 1.5e11 viral genomes of enhancer-AAV virus, diluted with 1X
670 PBS to a total volume of 10 μ L, unilaterally into the forebrain lateral ventricle (ICV delivery) with a 31-
671 gauge, 4 point, 12° bevel 1 inch needle (custom ordered from Hamilton) and 25 μ L capacity removable
672 needle syringe (Hamilton, 7636-01). Between injections we washed the needle and syringe with 100%
673 ethanol, and then nuclease-free water. We targeted the ICV space at 2 mm posterior to bregma, 2 mm
674 lateral to the anterior-posterior midline, and at a depth of 2 mm perpendicular to the surface of the skull.
675 We injected into the ventricle slowly over approximately 30 seconds. After injection, we held the needle
676 in place for approximately 10 seconds to prevent viral leakage, then slowly withdrew the needle at the
677 same relative angle as injection and then placed the animal onto a prewarmed heating pad in a clean
678 cage. We sacrificed pups at 18 days post injection, prior to weaning, and transcardially perfused with
679 1X PBS and then 4% PFA in PBS. We hemisected each brain and cryoprotected in 30% sucrose in
680 deionized water for a minimum of 24 hours before sectioning. We sectioned each brain at 30 μ m
681 thickness using a sliding microtome (Leica part number SM2000R) on a leveled mount of Tissue-Tek®
682 O.C.T. Compound, collecting 3 sagittal planes separated by approximately 500 μ m. We counterstained
683 sections with 1 μ g/mL DAPI and 2.5 μ g/mL propidium iodide (Thermo catalog # P1304MP) overnight at
684 4°C and mounted in VECTASHIELD® HardSet™ Antifade Mounting Medium prior to imaging by
685 epifluorescence.

686 *NHP enhancer-AAV testing.* NHP animals were housed and injected at the Washington National
687 Primate Center according to NIH guidelines and as approved by the University of Washington Animal
688 Care and Use Committee under UW IACUC protocol #41-6701. These animals received several
689 intraparenchymal injections under general anesthesia at spatially distinct sites located at least ~1cm
690 apart throughout the brain. During injection, over the course of 10 minutes we expelled a total of
691 approximately 1e11 gc iodixanol gradient-purified PHP.eB-packaged viral vectors in a total volume of 5
692 μ L at 10 depths ranging from 200 to 2000 microns deep in the animals. After injection the animal rested
693 for 10 minutes between injections. These numbers are approximate and timing, volume, and depths,
694 may be adjusted according to animal anatomy and surgical considerations. The experiments described
695 here result from two injection sites in one male *Macaca nemestrina* animal. We harvested tissue from
696 this animal after necropsy at 113 days post injection.

697 After locating the injection sites and cutting out tissue blocks about 1-2cm on each side surrounding the
698 injection sites, we fixed these tissue blocks in 4% PFA for 24 hrs. Then we rinsed the blocks with PBS,
699 cut 350 μ m thick slices on the sliding microtome, and postfixated the slices in 4% PFA for 2 hours at
700 room temperature (RT), washed three times in PBS for 10 min each, then transferred to 70% EtOH at
701 4°C for a minimum of 12 hours, and up to 30 days.

702 For ISH analysis we first incubated the slices in 8% SDS in PBS at RT for two hours with agitation, then
703 washed the slices at RT with 5X sodium chloride sodium citrate (SSC) for three hours, exchanging with
704 fresh 5X SSC every hour. Next we performed HCR v3.0 using reagents and a modified protocol from
705 Molecular Technologies and Molecular Instruments⁸⁵. We first incubated slices in pre-warmed 30%
706 probe hybridization buffer (30% formamide, 5X sodium chloride sodium citrate (SSC), 9 mM citric acid
707 pH 6.0, 0.1% Tween 20, 50 µg/mL heparin, 1X Denhardt's solution, 10% dextran sulfate) at 37°C for 5
708 min. Then we exchanged hybridization buffer for hybridization buffer containing probes added at a
709 concentration of 2 nM. Molecular Instruments designed the probes using the following accession
710 numbers: SLC17A7 – XM_011768126.1, GAD1 – XM_011744029.1, FGFR3 – XM_011744842.2,
711 SOX10 – XM_011712410.2. Hybridization proceeded overnight at 37°C, and afterwards we washed the
712 tissue thrice with 5X SSC for 10 minutes each (total 30 minutes), then 30% probe wash buffer (30%
713 formamide, 5X SSC, 9 mM citric acid pH 6.0, 0.1% Tween 20, 50 µg/mL heparin) for one hour at 37°C.
714 Then we exchanged probe wash buffer with 5X SSC, then amplification buffer (5X SSC, 0.1% Tween
715 20, 10% dextran sulfate) for 5 min at room temperature. Meanwhile we pooled even and odd
716 amplification hairpins for each of the three genes and snap-cooled them by heating to 95°C for 90
717 seconds then cooling to room temperature for 30 min, and afterwards we added the snap-cooled
718 hairpins to amplification buffer at a final concentration of 60 nM, and finally centrifuged at 18000g for 1
719 minute. Then we incubated tissue slices in amplification solution containing amplification hairpins for 4
720 hours at room temperature, followed by staining in DAPI (10µg/mL in 2X SSC) for 1 hour at room
721 temperature, and finally washing twice for 30 min in 2X SSC at room temperature before imaging. We
722 prepared a fresh aliquot of 67% 2,2'-Thiodiethanol (TDE) solution for use as a clearing and immersion
723 fluid by mixing ≥99% TDE (Sigma-Aldrich) with deionized water to create a 67% TDE solution with a
724 refractive index of 1.46. We transferred slices to 67% TDE and allowed them to equilibrate for at least 1
725 hour at room temperature prior to imaging on a confocal microscope (Olympus FV-3000).

726 *Stereotaxic injection and fiber implant surgery.* Virus injection and optic fiber implantation surgery was
727 performed in C57BL/6J mice (The Jackson Laboratory, #000664) at around P60. Mice were
728 anesthetized with isoflurane and monitored throughout the surgery using breathing rate and tail pinch.
729 The skin above the skull surface was removed to make room for the fiber implant and headframe. After
730 leveling the skull, a craniotomy was drilled above the injection and fiber coordinates (AP: 1.2 mm, ML: -
731 1.3 mm, DV: 4.1 mm). First, a glass pipette positioned at the injection coordinates was lowered through
732 the craniotomy and virus injection was performed (100 nl, titer: 4E13). Once the injection was complete,
733 the pipette was slowly raised, and the optic fiber probe was position at the same AP and ML
734 coordinates as the injection. The tip of the fiber was then lowered to 100 µm above the injection site
735 and glued in place where the base of the fiber ferrule contacts the skull. A custom headframe was then
736 glued to the skull to allow head-fixed behavior and imaging. After surgery, the mouse was returned to
737 the home cage and allowed to recover for at least two weeks prior to start of water restriction for
738 behavior and imaging.

739 *Dynamic foraging reinforcement learning task.* Water-restricted and head-restrained mice were trained
740 to perform a reinforcement learning task where they freely choose between two lick ports that delivered
741 a water reward with nonstationary probabilities. This is a variation on the task described in Bari et al.⁸⁶.
742 The base reward probability of both lick ports summed to 0.6 where the probabilities of the two lick

743 ports were selected from two sets of ratios (0.53/0.07, 0.51/0.09). Block lengths that corresponded to
744 each ratio lasted for about 30 trials (min trials per block: 40, max trials per block: 60). Each trial began
745 with an auditory “go cue” that signaled the start of a trial. The mouse was free to choose between the
746 left or right lick port immediately after the “go cue”. The trials were separated by a variable inter-trial-
747 interval (range between 1-7 seconds). The data shown in this study was from a two-hour behavior
748 session that consisted of 438 trials (170 rewarded trials).

749 *Fiber photometry and analysis.* Fiber photometry was performed using a commercially available
750 photometry system (Neurophotometrics LLC, FP3002). A 470 nm LED was used to excite the
751 iAChSnFR fluorophore, Venus, and the emitted fluorescence signals were collected using a CMOS
752 camera. The 470 nm excitation was interleaved with a 415 nm LED as an isosbestic control to remove
753 motion artifacts. Bonsai acquisition software was used to record the photometry signals as well as the
754 behavior trigger signals events (go-cue, left and/or right lick choices, reward/no reward) for offline
755 alignment of imaging data to behavioral events. Prior to start of acquisition, an ROI was drawn over the
756 fiber image seen on the camera, and fluorescence intensity within this ROI was averaged for real-time
757 signal visualization and offline analysis. First, the fiber photometry acquisition was started, following
758 which the behavior task was initialized. Photometry signals were analyzed using custom python scripts.
759 First, the fluorescence signal was detrended for photobleaching using a fourth order polynomial
760 function and then corrected for motion using the control signal from the 415 nm excitation using
761 standard photometry analysis techniques⁸⁷. Acetylcholine signal changes were calculated as a change
762 in fluorescence intensity over the mean fluorescence ($\Delta F/F$ as a percentage). The photometry signals
763 were then aligned to behavior events using simultaneously acquired TTL readouts of behavior events
764 (go-cue, left and/or right lick choices, reward/no reward) using a NI USB card. These behavior events
765 were then used to calculate trial averaged traces of rewarded and unrewarded signals.

766

767 **Data Availability:**

768 All AAV viral vector plasmids will be made freely available for research use at Addgene (addgene.org/).
769 Mouse scRNA-seq generated from this study will be made available at GEO with the accession number
770 GSE235987 (<https://www.ncbi.nlm.nih.gov/geo/>). Mouse serial two photon tomography datasets will be
771 made available through the Brain Imaging Library (<https://www.brainimaginglibrary.org/>). All other data
772 will be made available upon request.

773 **Ethics Declarations:**

774 Competing interests

775 Several authors including ESL, JTT, JKM, RAM, XOA, BT and BPL are inventors on one PCT stage
776 patent application (PCT_US2021_024525) and one provisional patent covering vectors described in
777 this manuscript. BPL is a scientific advisor for Patch Bioscience.

778 **Acknowledgements**

779 We would like to thank the Washington National Primate Center and staff for animal care, as well as the
780 supporting grant P51OD010425 from the National Institutes of Health to support NHP research. The
781 WaNPRC SPF *M. nemestrina* colony is supported by grant U42OD011123 from the NIH Office of
782 Research Infrastructure Programs. We would like to acknowledge Kathryn Gudsnuk for programmatic
783 support. This work was supported by the following grants: RF1MH114126-01 from the National Institute
784 of Mental Health to BPL, JTT, and ESL; UG3MH120095-01, -02, -03 from the National Institute of
785 Mental Health to BPL, JTT, ESL, and FKK, UF1MH128339-01 from the National Institute of Mental
786 Health to BT, TB, TLD, BPL, and JTT, RF1MH121274-01 from the National Institute for Mental Health
787 to BT and U19MH114830 to HZ. We also would like to acknowledge the estate of Paul G. Allen for his
788 vision, encouragement, and support.

789 **Figures and Figure Legends**

790

791 **Figure 1: Astrocyte and oligodendrocyte enhancer discovery from single cell epigenetics.**

792

793 (A) Example astrocyte- and oligodendrocyte-specific peaks near the loci of astrocyte-specific gene
794 *AQP4* and oligodendrocyte-specific gene *OPALIN*, identified in human MTG snATAC-seq data³⁵.

795 (B) Differing approaches to identify candidate enhancers. Specific accessibility peaks are depicted as
796 peaks, and specifically demethylated regions are depicted as troughs. Schemes not utilizing a particular
797 data modality are shown as “Agnostic”. Marker gene selection criteria can use accessibility from either
798 mouse or human. Icons represent identification schemes; gold star candidate enhancers undergo more
799 stringent criteria than those with gold squares (see Methods for details).

800 (C) Workflow for enhancer cloning, packaging, screening, and validation. Enhancers are cloned into a
801 pAAV plasmid upstream of a minimal human beta-globin promoter and SYFP2 reporter, and plasmids
802 are packaged into PHP.eB AAVs. Enhancer-AAVs are injected intravenously into retro-orbital sinus,
803 and expression is assessed by imaging. Promising enhancer-AAVs then go on to secondary validation
804 experiments consisting of cross-species validation, molecular characterization by IHC and/or
805 multiplexed FISH, and flow cytometry for single cell RNA-seq.

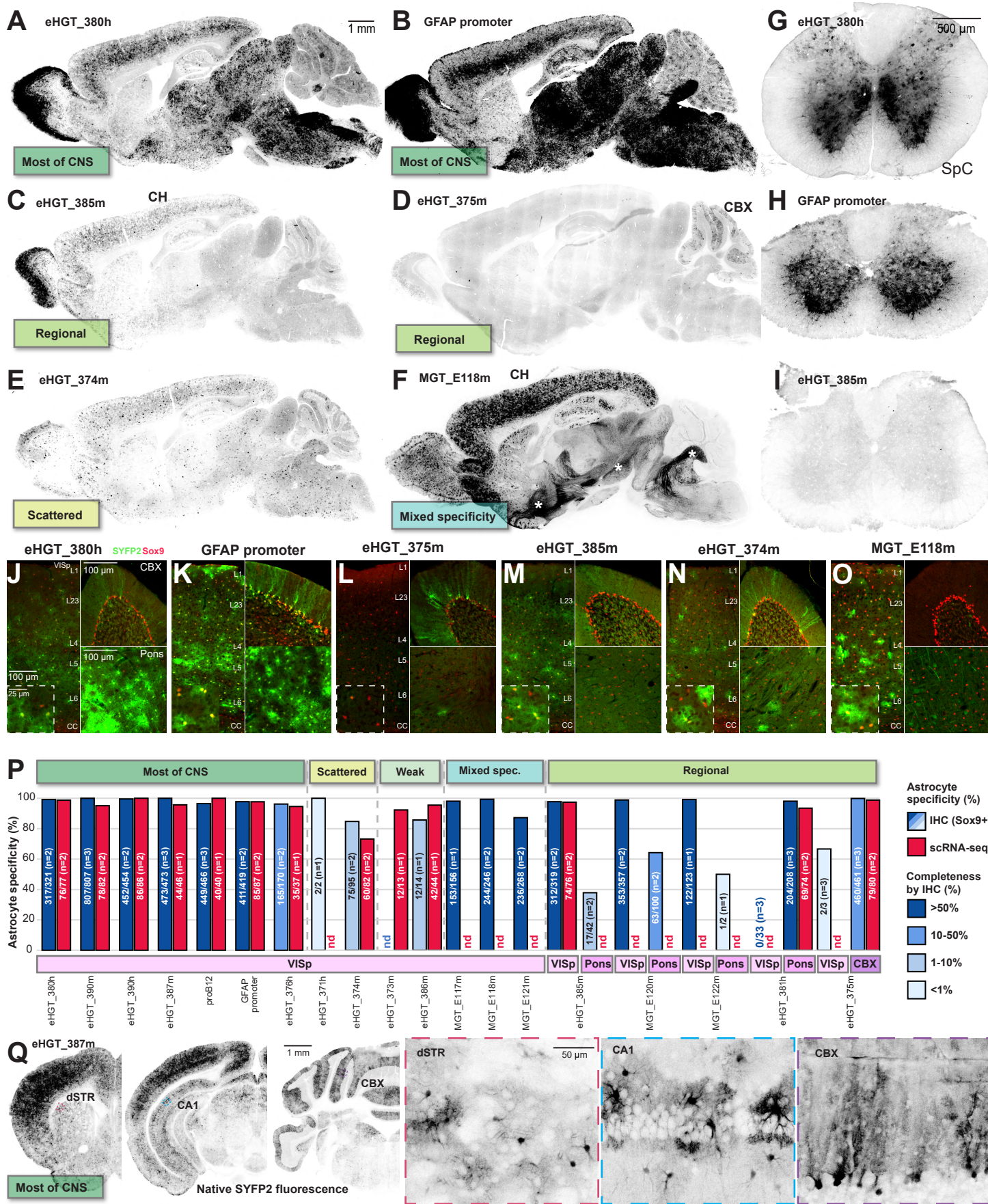
806 (D-E) Accessibility profiles of candidate mouse astrocyte-specific (D) and oligodendrocyte-specific
807 enhancers (E). For each genomic region we show their peak nomination scheme matching to Figure
808 1B, enhancer name, and enhancer accessibility profile transformed to CPM in mouse VISp scATAC-
809 seq dataset³⁶.

810 (F-G) Summarized screening results. Overall, we observed high success rates of tested enhancer-
811 AAVs giving specific astrocyte or oligodendrocyte expression patterns. Testing result bar: Y = yes,
812 enhancer-AAV gives strong or moderate on-target expression pattern; N = no, enhancer-AAV fails to
813 express; W = weak on-target expression pattern; Mx = mixed expression pattern consisting of on-target
814 cells plus unwanted neuronal populations; Off = off-target expression pattern; ND = no data. Note both
815 enhancers giving strong/moderate (“Y”) and weak (“W”) specific expression are grouped here for
816 overall success rate analysis.

817

818

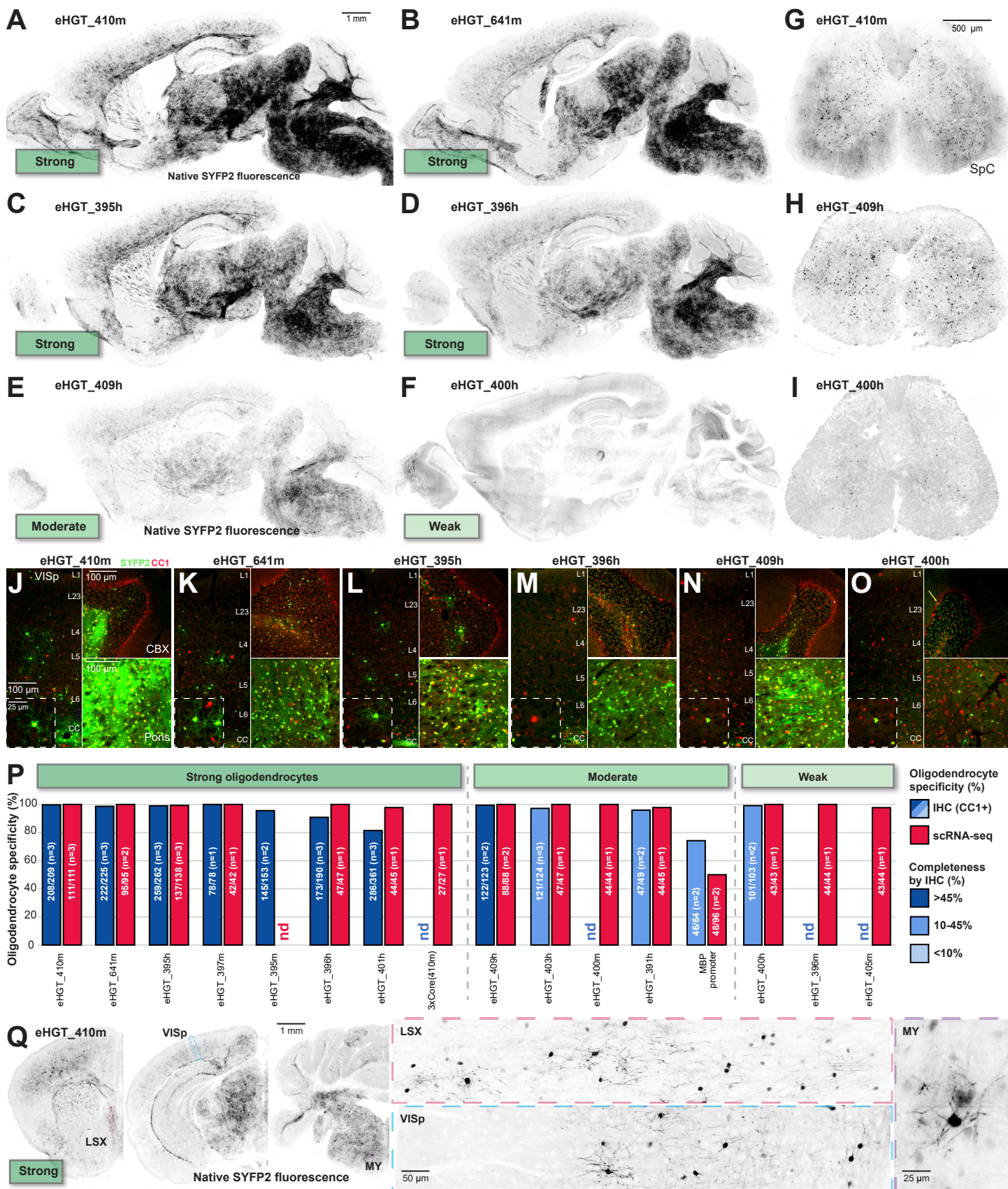
819



820 **Figure 2: A collection of astrocyte-specific enhancer-AAV vectors with varying regional**
821 **specificities and expression densities.**

- 822
823 (A-B) Astrocyte-specific enhancer-AAVs marking many astrocytes throughout most of the CNS.
824 eHGT_380h (A) and *GFAP* promoter (B) mark many astrocytes throughout gray matter in FB, MB, HB,
825 and CBX.
- 826 (C-D) Astrocyte-specific enhancer-AAVs marking many astrocytes in isolated regions of the brain. (C)
827 eHGT_375m specifically labels cerebellar (CBX) Bergmann glia but not FB, MB, or HB. (D)
828 eHGT_385m labels astrocytes in cerebrum (CH) but not in MB, HB, or CBX.
- 829 (E) Astrocyte-specific enhancer-AAV eHGT_374m marking scattered astrocytes. These scattered
830 astrocytes are located throughout FB, MB, HB, and CBX.
- 831 (F) Mixed specificities from astrocyte enhancer MGT_E118m. MGT_E118m labels astrocytes in the
832 cerebrum (CH) but also off-target neuron populations in deep cerebellar nuclei, midbrain, and globus
833 pallidus, external segment (marked by asterisks).
- 834 (G-I) Astrocyte-specific enhancer-AAVs labeling astrocytes in lumbar SpC. eHGT_380h (G) and *GFAP*
835 promoter (H) label many astrocytes in SpC gray matter, but eHGT_385m (I) does not label SpC
836 astrocytes.
- 837 (J-O) Positive confirmation of molecular astrocyte identity across brain regions. SYFP2+ astrocytes are
838 colabeled with anti-Sox9 immunoreactivity in VISp, CBX, and Pons.
- 839 (P) Quantification of specificity for astrocytes by astrocyte enhancer-AAVs. Specificity and
840 completeness for astrocyte labeling by enhancer-AAVs was quantified by costaining with anti-Sox9
841 antibody in VISp, Pons, and CBX. Specificity is defined as the number of SYFP2+Sox9+ / total SYFP2+
842 cells x 100%. Completeness is defined as the number of SYFP2+Sox9+ / total Sox9+ cells x 100%.
843 Brains from one to three mice per condition were analyzed, with range 131-827 cells counted (median
844 311) per brain region analyzed. eHGT_375m-labeling was only quantified in the Purkinje cell layer of
845 CBX, not in the granule or molecular layers. Specificity was also quantified by scRNA-seq, defined as
846 the percentage of sorted SYFP2+ cells mapping as astrocytes within the VISp molecular taxonomy⁸³.
847 Overall, specificity is high for many astrocyte-specific vectors, with “Scattered” and “Weak” vectors
848 showing low completeness, and “Regional” vectors showing more completeness in certain regions.
- 849 (Q) Distinct astrocyte morphologies throughout the brain with eHGT_387m enhancer-AAV targeting
850 “Most of CNS”. Images were acquired on a serial blockface imaging platform (TissueCyte).
- 851 Abbreviations: CH cerebrum, dSTR dorsal striatum, CA1 cornu ammonis 1, CBX cerebellar cortex, SpC
852 spinal cord, VISp primary visual cortex.

853
854



855 **Figure 3: A collection of oligodendrocyte-specific enhancer-AAV vectors with varying levels of**
856 **expression.**

857

858 (A-F) Oligodendrocyte enhancer-AAVs marking many oligodendrocytes throughout most of the CNS.
859 eHGT_410m (A), eHGT_641m (B), eHGT_395h (C), eHGT_396h (D), eHGT_409h (E), and
860 eHGT_400h (F) label many oligodendrocytes throughout FB, MB, HB, and CBX, but at differing
861 expression levels.

862 (G-I) Oligodendrocyte enhancer-AAVs marking oligodendrocytes in lumbar SpC. eHGT_410m (G),
863 eHGT_409h (H), and eHGT_400h (I) mark oligodendrocytes in gray and white matter of SpC, but at
864 different intensities.

865 (J-O) Positive confirmation of molecular oligodendrocyte identity across brain regions. SYFP2+
866 oligodendrocytes are colabeled with CC1 immunoreactivity in VISp, CBX, and Pons.

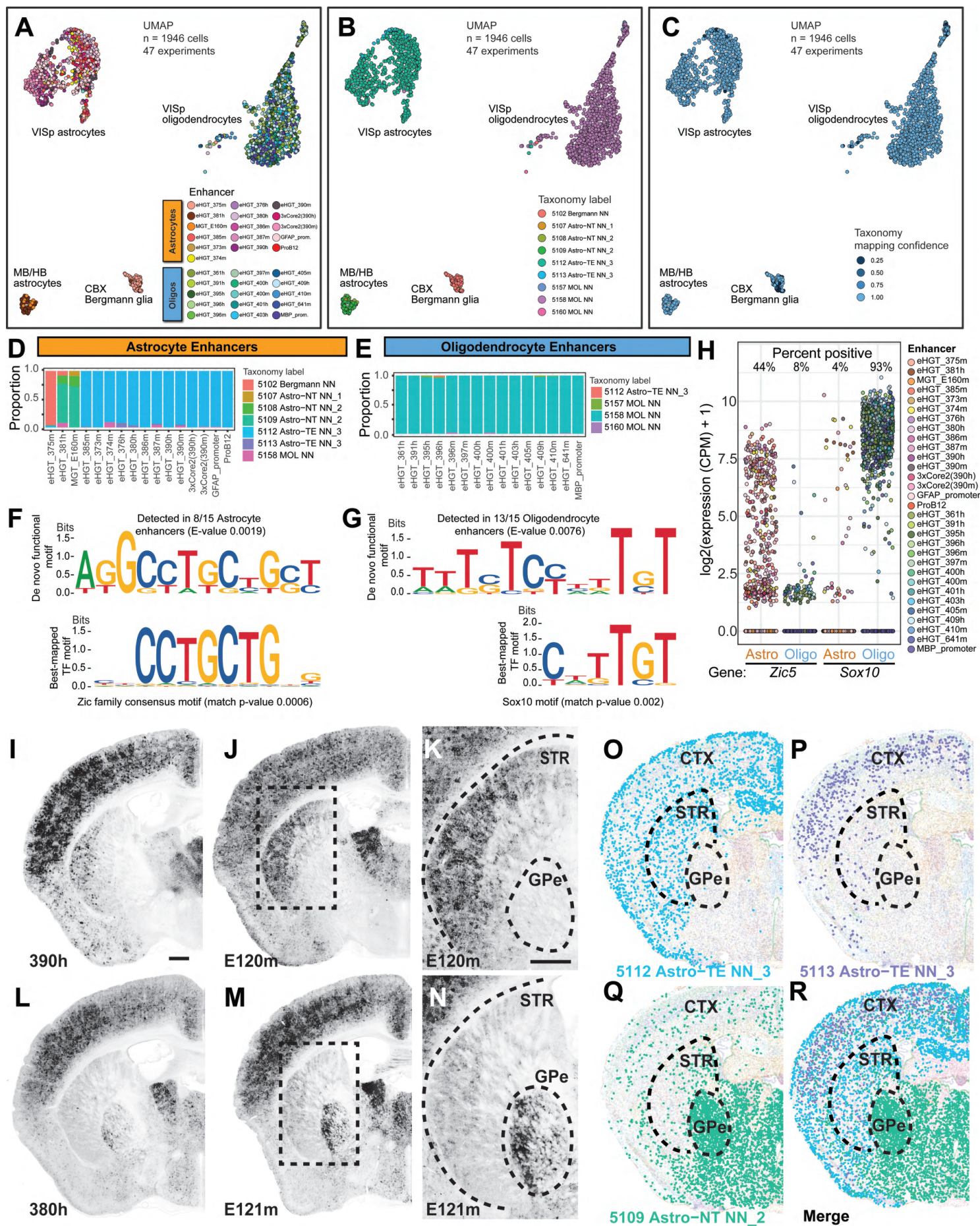
867 (P) Quantification of specificity for oligodendrocytes by oligodendrocyte enhancer-AAVs. Specificity and
868 completeness for oligodendrocyte labeling by enhancer-AAVs was quantified by costaining with CC1
869 antibody in VISp, Pons, and CBX. Specificity is defined as the number of SYFP2+CC1+ / total SYFP2+
870 cells x 100%. Completeness is defined as the number of SYFP2+CC1+ / total CC1+ cells x 100%.
871 Brains from one to three mice per condition were analyzed, with range 101-332 cells counted (median
872 147) per brain region analyzed. Specificity was also quantified by scRNA-seq, defined as the
873 percentage of sorted SYFP2+ cells mapping as oligodendrocytes within the VISp molecular
874 taxonomy⁸³. Overall, specificity is high for many oligodendrocyte-specific vectors, with “Weak” vectors
875 showing low completeness.

876 (Q) Myelinating oligodendrocyte morphologies throughout the brain with eHGT_410m. Sections were
877 visualized with serial blockface imaging on the Tissuecyte platform.

878 Abbreviations: SpC spinal cord, VISp primary visual cortex, CBX cerebellar cortex, LSX lateral septal
879 complex, MY medulla.

880

881



882 **Figure 4: Transcriptomic identities of prospectively targeted astrocytes and oligodendrocytes.**

883

884 (A-C) Groups of transcriptomically profiled single cells, as visualized by UMAP. Single cells labeled by
885 various astrocyte- and oligodendrocyte-specific enhancer-AAVs (n = 1946 quality-filtered cells) were
886 profiled from 47 brains in 47 independent experiments by SMARTerV4⁸³. Libraries were aligned to
887 mm10 and transformed into UMAP space for visualization, with coloring by enhancer (A), mapped
888 taxonomic cell type cluster (B), and taxonomic mapping confidence (C). Overall CTX astrocytes group
889 away from CTX oligodendrocytes as expected, and MB/HB astrocytes and Bergmann glia astrocytes
890 group away from CTX astrocytes, consistent with recent results²⁰. Note that eHGT_381h- and
891 MGT_E160m-labeled astrocytes were dissected from MB/HB region, and eHGT_375m-labeled
892 Bergmann glia were dissected from CBX region, but the remainder of the cells were dissected from
893 VISp.

894 (D-E) Quantifications of taxonomic cell type cluster mapping by enhancer vector. Prospectively labeled
895 astrocytes from all enhancer-AAV vectors dissected from VISp predominantly map to cluster “5112
896 Astro-TE NN_3”, whereas those from MB/HB dissections (eHGT_381h and MGT_E160m)
897 predominantly map to cluster “5109 Astro-NT NN_2”, and eHGT_375m-labeled astrocytes from CBX
898 dissections predominantly map to cluster “5102 Bergmann NN”. In contrast, all prospectively labeled
899 oligodendrocytes predominantly map to cluster “5158 MOL NN”. Cluster identities are from a recent
900 whole mouse brain taxonomy study²⁰.

901 (F-H) De novo motif detection in astrocyte- and oligodendrocyte-specific enhancer sequences using
902 MEME-CHIP⁵⁶ identifies one strong consensus motif in each set of sequences (top). These de novo
903 motifs were mapped against databases of known TF motifs using TomTom (bottom), which identified
904 the top hits as the Zic family consensus motifs for astrocytes, and Sox family motif for oligodendrocytes
905 (Sox10 shown). These TFs (Zic5 and Sox10) show highly specific expression differences between
906 astrocytes and oligodendrocytes from prospective scRNA-seq profiling (H).

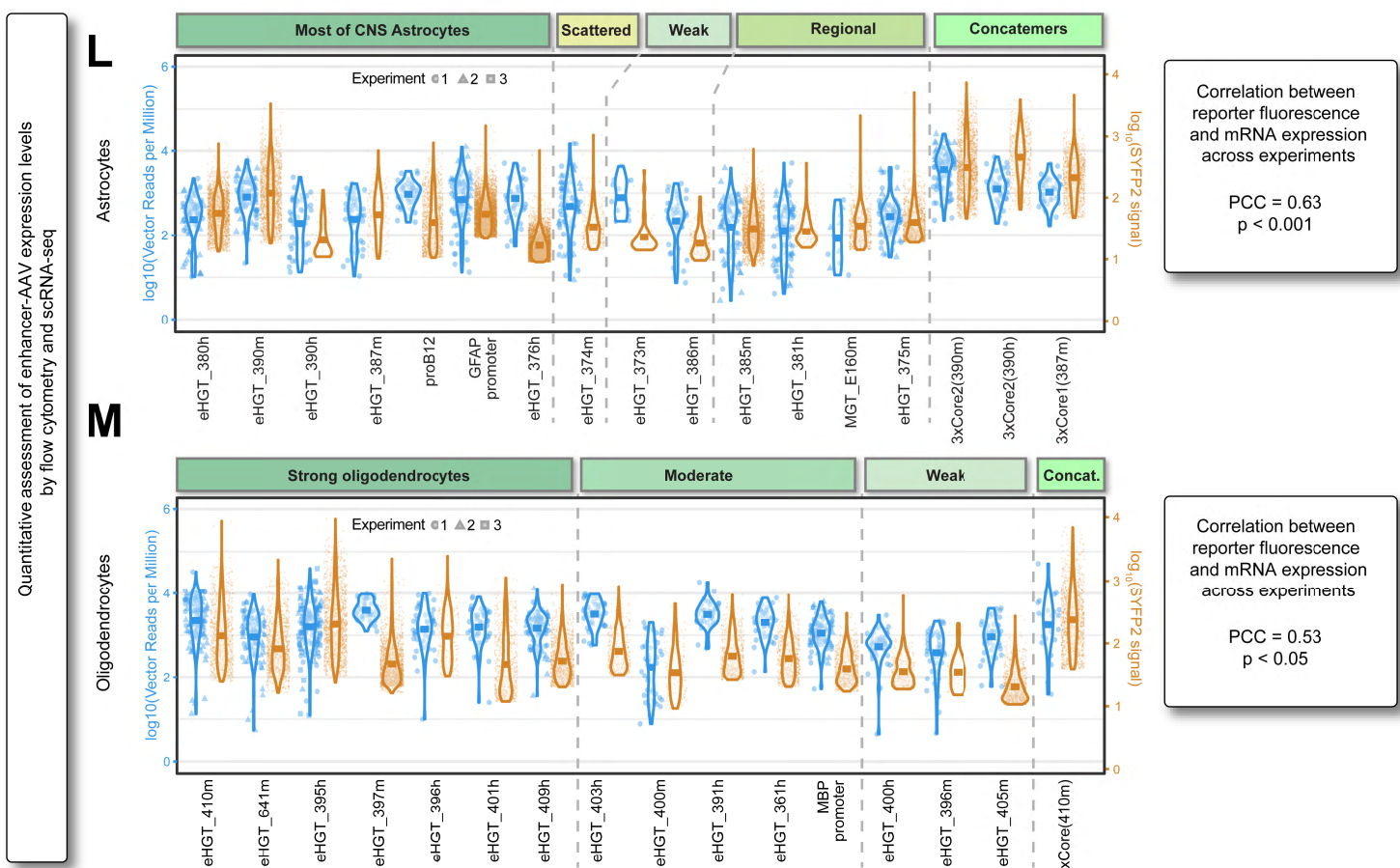
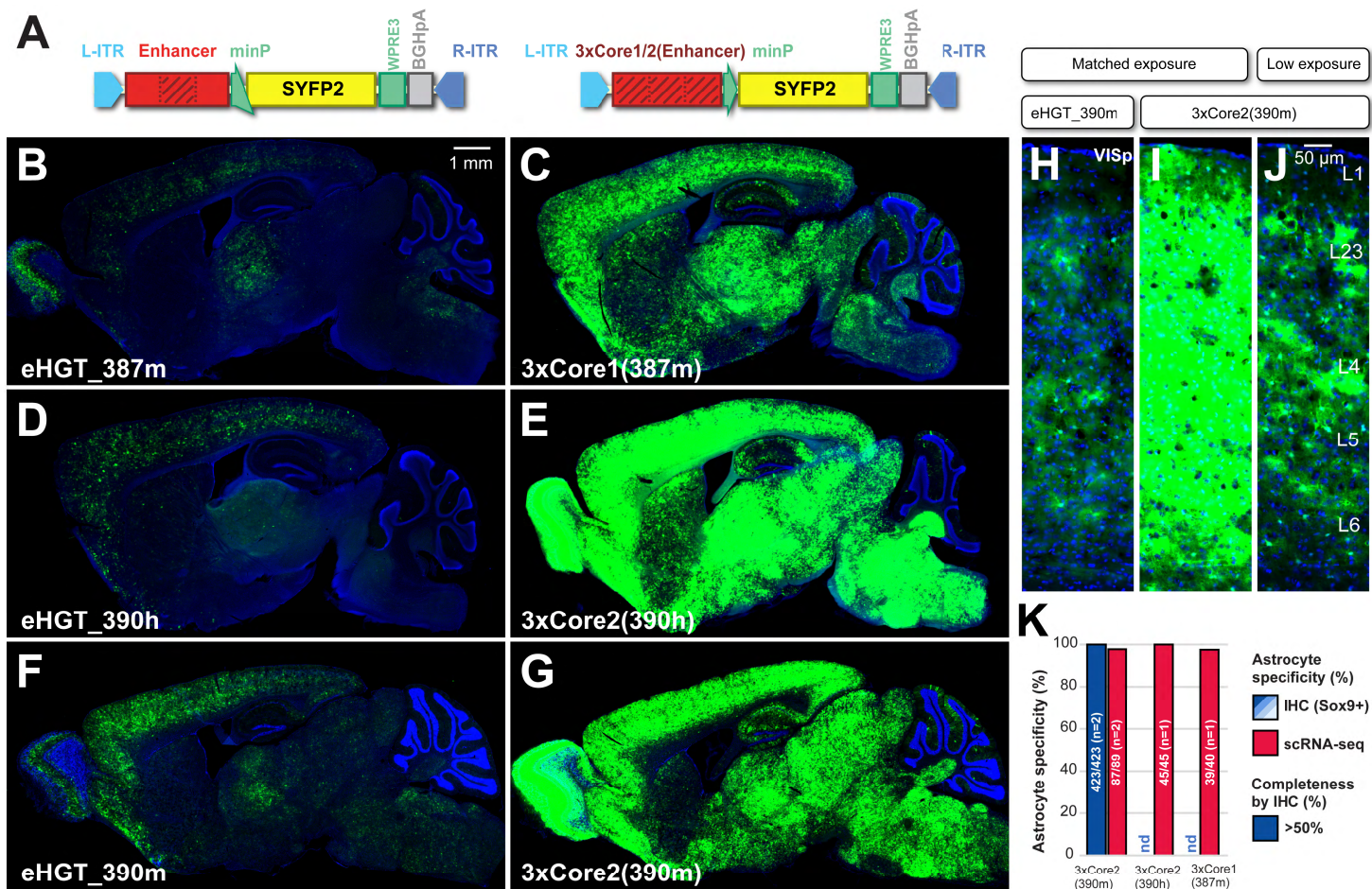
907 (I-N) Intrinsic SYFP2 expression from the indicated enhancer-AAVs after retro-orbital administration.
908 Images were generated by STPT. Boxes in I and L correspond to K and N, respectively. Scale in I and
909 K is 500 μ m.

910 (O-R) MERFISH data showing the distribution of three astrocyte cell types revealed by single cell gene
911 expression from the whole mouse brain²⁰.

912 Abbreviations: CTX cerebral cortex, STR striatum, GPe globus pallidus, external segment.

913

914



915 **Figure 5: Optimizing astrocyte and oligodendrocyte enhancer strength.**

916

917 (A) Native Enhancer and for 3xCore2(Enhancer) vector designs. The central approximate third of the
918 enhancer (the “Core2” element) is marked by dark hatches, and this element is triply concatemerized in
919 the 3xCore2(Enhancer) vector. Alternatively, the first or third segment (“Core1” or “Core3”) may be
920 concatemerized (determined empirically).

921 (B-J) Dramatic increase in expression levels while maintaining specificity using 3xCore1/2(Enhancer)
922 vector designs. Brains from mice injected with the Enhancer or 3xCore1/2(Enhancer) vectors were
923 processed and imaged in parallel in these experiments. (H-J) Zoom in view of eHGT_390m- and
924 3xCore2(390m)-injected mouse VISp shows high specificity for morphological astrocytes throughout
925 cortical layers in both cases.

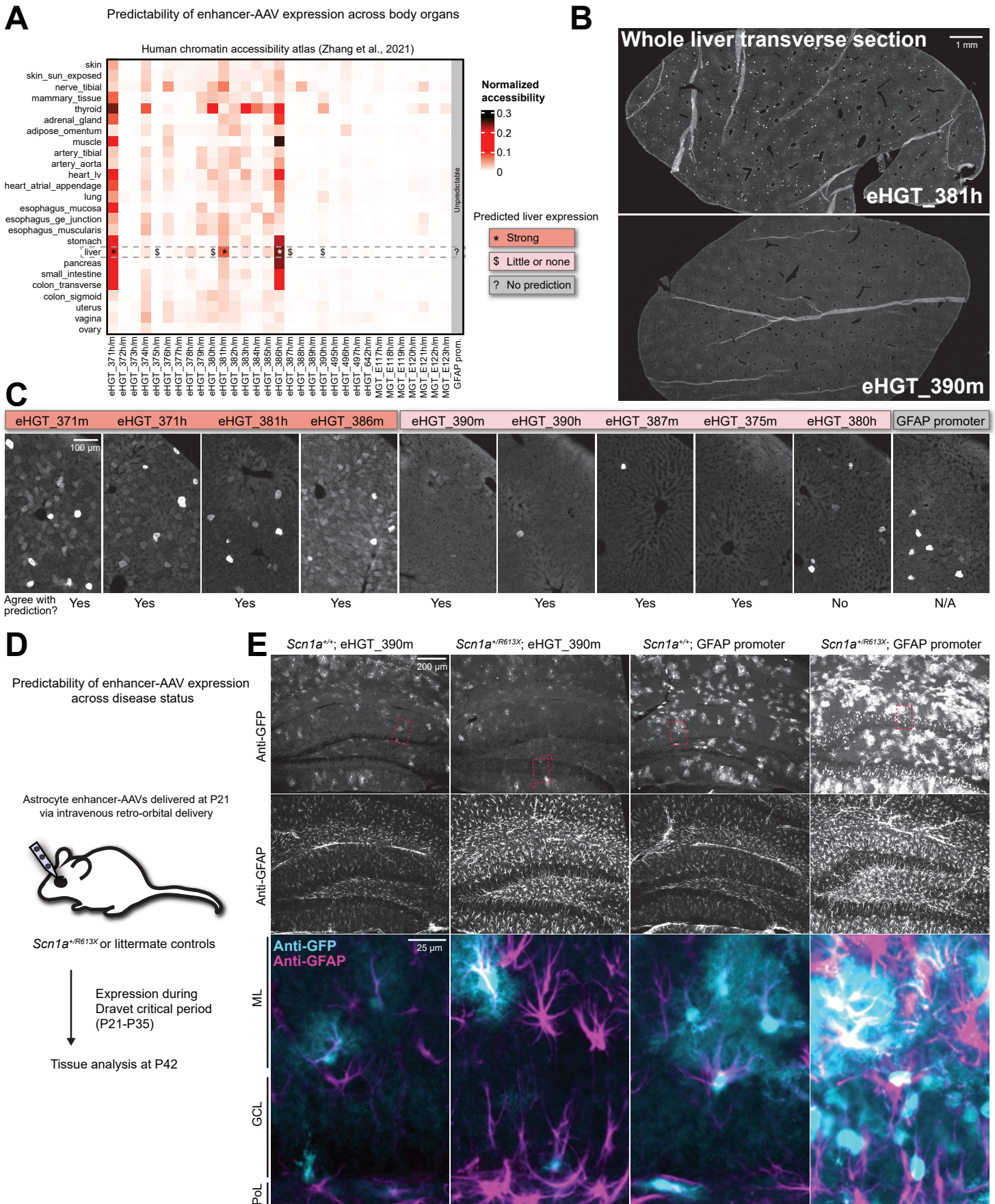
926 (K) Quantification of specificity for astrocytes by concatemer astrocyte enhancer-AAVs within VISp by
927 IHC and scRNA-seq as described in Figure 2P.

928 (L-M) Direct correlated quantification of enhancer strength by flow cytometry and scRNA-seq, for both
929 astrocyte- (L) and oligodendrocyte-specific (M) enhancer-AAVs. The left (blue) y-axis represents the
930 log-transformed vector transgene reads per million in individual sorted scRNA-seq-profiled cells. The
931 right (brown) y-axis represents the log-transformed SYFP2 signal intensity of positively gated vector-
932 expressing cells observed on the flow cytometer, quantified as the fold signal of positive cells
933 normalized to non-expressing cell autofluorescence (taken as background). Points represent individual
934 cells observed by scRNA-seq and by flow cytometry, visualized also as violins, and with the horizontal
935 bar representing mean expression levels across all cells expressing that enhancer-AAV, across one to
936 three replicate experiments per vector. Across all experiments, we observe significant correlation
937 between mean expression intensity at the RNA level by scRNA-seq, and mean SYFP2 reporter
938 expression by signal intensity (astrocytes: $n = 26$ experiments, Pearson correlation coefficient [PCC]
939 0.63 , $t = 3.97$, $df = 24$, $p = 0.00057$; oligodendrocyte $n = 22$ experiments, PCC 0.53 , $t = 2.82$, $df = 20$, p
940 $= 0.011$). Furthermore, 3xCore astrocyte enhancers are among the strongest enhancers we have
941 characterized, typically several fold stronger than their native counterparts.

942 Abbreviations: VISp primary visual cortex.

943

944



945 **Figure 6: Predictability of astrocyte enhancer-AAV expression patterns across body organs and**
946 **across disease states.**

947
948 (A) Accessibility profiles of astrocyte-specific enhancers in the human whole-body accessibility atlas⁶⁵.
949 Single-cell profiles were grouped within each tissue into pseudo-bulk aggregates, then normalized
950 according to the signal (reads in peaks) within the dataset. Accessibility profiles are likely to predict
951 enhancer activities within each tissue. Focusing on liver, some astrocyte-specific enhancers are
952 predicted to have high expression, and some are predicted to have very little or no expression. In
953 contrast, accessibility atlases do not predict expression of *GFAP* promoter across tissues.

954 (B) Whole livers from mice injected intravenously with eHGT_381h- and eHGT_390m-enhancer-AAV
955 vectors, stained with anti-GFP antibody. eHGT_381h has high liver accessibility, is predicted to have
956 high liver expression, and shows many strong SYFP2-expressing hepatocytes throughout the liver as
957 predicted. In contrast, eHGT_390m has very little liver accessibility and so is predicted to have little
958 liver expression, and in fact shows few positive SYFP2-expressing hepatocytes as predicted.

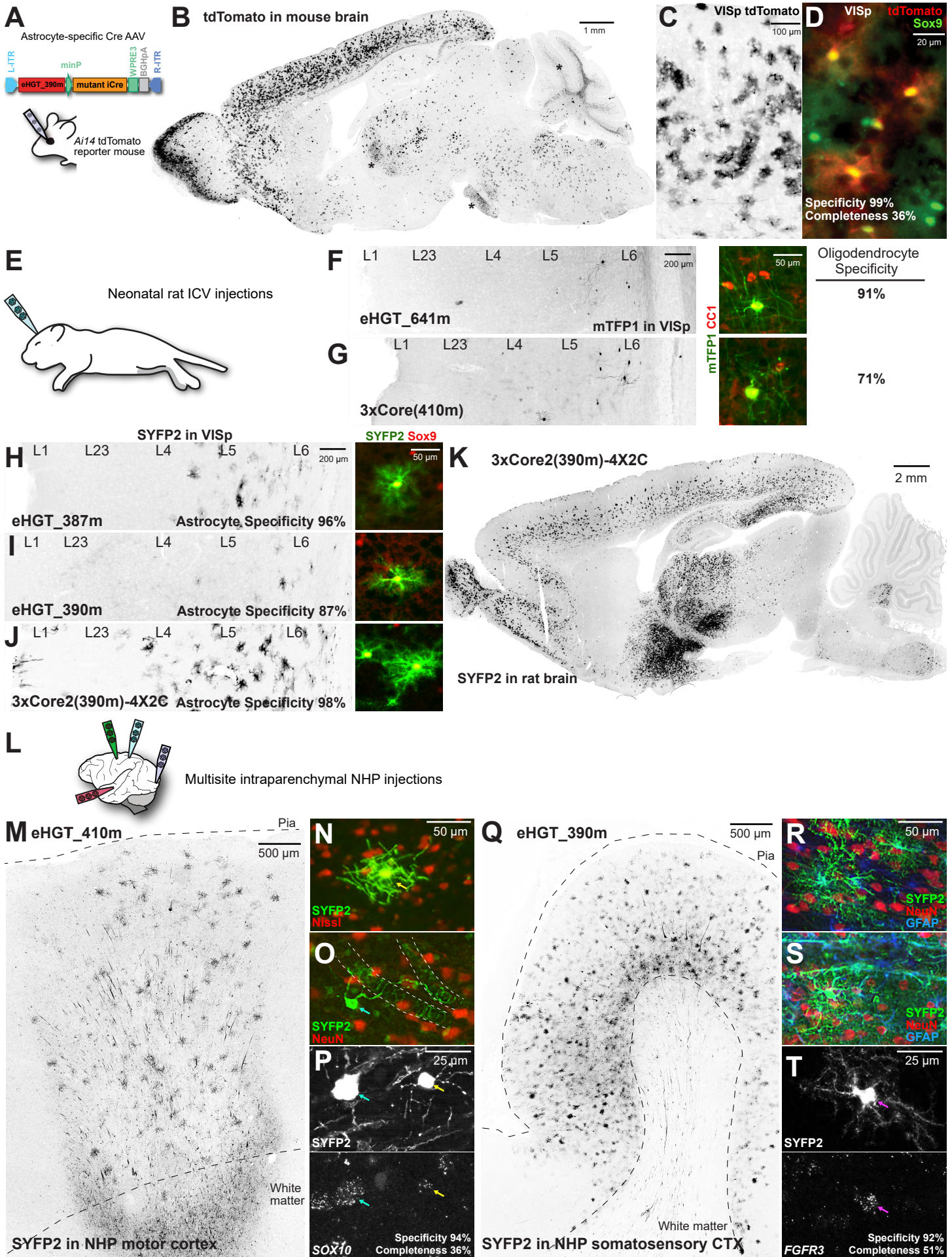
959 (C) Agreement between liver expression predictions and liver expression measurements across several
960 astrocyte-specific enhancer-AAV vectors. eHGT_371m, 371h, 381h, and 386m all show many SYFP2-
961 expressing hepatocytes as predicted. eHGT_390m, 390h, 375m, and 387m show few weak SYFP2-
962 expressing hepatocytes as predicted. *GFAP* promoter shows many expressing hepatocytes, which was
963 not predictable from the accessibility atlases. eHGT_380h shows many SYFP2-expressing astrocytes,
964 in contrast to the epigenetic prediction. Liver images in B and C represent one to two mice analyzed for
965 each vector.

966 (D-E) Testing fidelity of enhancer-AAV expression across disease states. We used a Dravet syndrome
967 model *Scn1a*^{R613X/+} mouse to induce epilepsy-associated hippocampal gliosis, injected enhancer-AAVs
968 prior to the critical period, and analyzed tissue for expression patterns after the critical period (D). We
969 assessed hippocampal gliosis with anti-GFAP antibody and enhancer-AAV expression with anti-GFP
970 antibody (E). eHGT_390m maintained specific expression and similar levels in hippocampal astrocytes
971 regardless of epileptic gliosis. In contrast, *GFAP* promoter expression strongly increased in gliotic
972 astrocytes, and also was observed in dentate gyrus granule cells. Red dashed rectangles indicate the
973 position of the expanded zoomed view, and the curved arrows indicate a rotated view.

974 Abbreviations: ML molecular layer, GCL granule cell layer, PoL polymorphic layer.

975

976



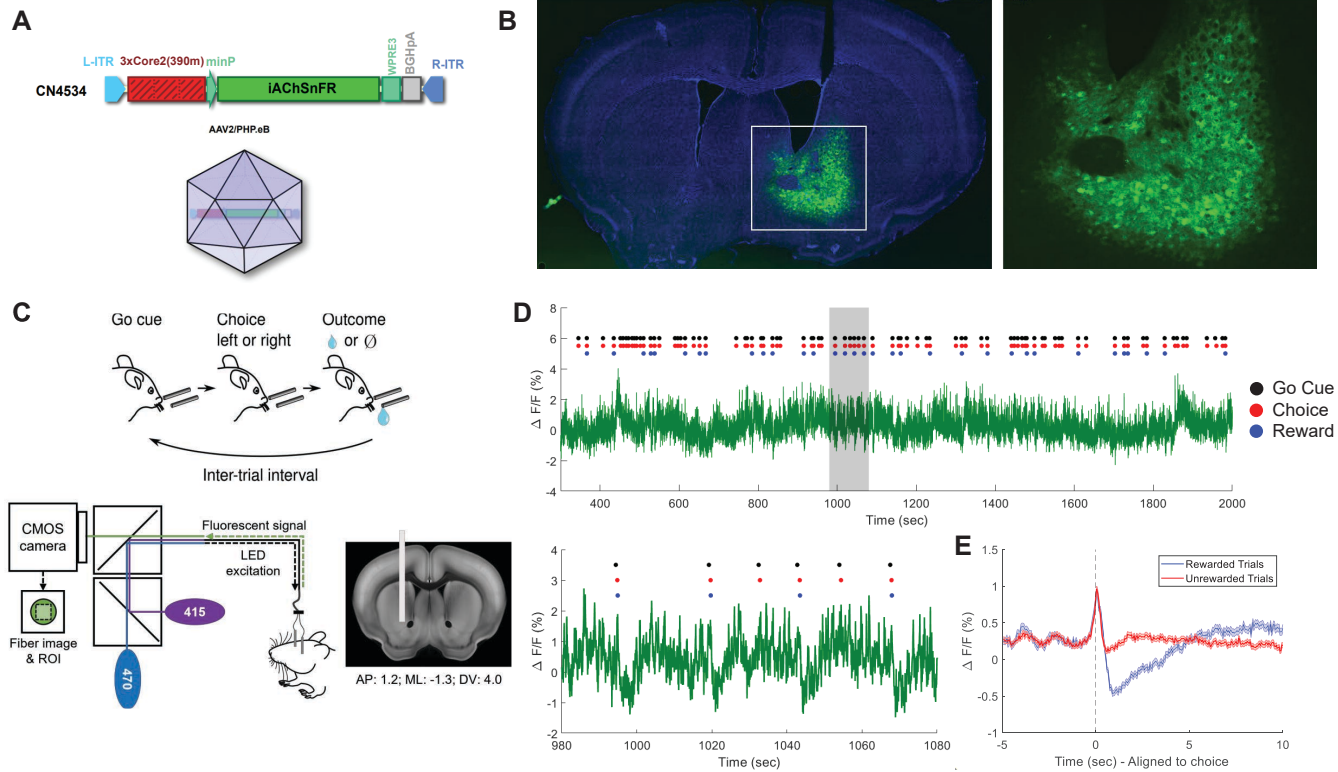
977 **Figure 7: Genetic targeting of astrocytes and oligodendrocytes with functional transgenes and**
978 **across species.**

- 979
980 (A) Design and testing of an astrocyte-specific mutant Cre-expressing enhancer-AAV.
- 981 (B-D) Specific recombination in astrocytes. Ai14 reporter recombination is observed in multiple parts of
982 mouse brain (B), except for a few regions with non-astrocyte recombination including thalamus, pontine
983 gray, and cerebellar granule layer (marked by asterisks). Recombination within cortex is highly specific
984 (C-D).
- 985 (E) Testing enhancer-AAV vectors by neonatal rat ICV injections.
- 986 (F-G) Validation of oligodendrocyte-specific enhancer-AAV vectors in rat. eHGT_410m and 641m show
987 specific expression in CC1+ VISp oligodendrocytes.
- 988 (H-J) Validation of astrocyte-specific enhancer-AAV vectors in rat. eHGT_387m, 390m, and
989 3xCore2(390m) show specific expression in Sox9+ VISp astrocytes. 3xCore2(390m) vector also
990 incorporates 4X2C 3'UTR miRNA binding sites to prevent any off-target labeling in excitatory neurons⁷⁰.
- 991 (K) 3xCore2(390m) with 4X2C 3'UTR miRNA binding sites⁷⁰ achieves widespread expression
992 throughout the rat forebrain.
- 993 (L) Multiple stereotactic intraparenchymal injections into NHP brain.
- 994 (M-P) Prospective labeling of NHP oligodendrocytes in vivo. eHGT_410m enhancer-AAV vector gives
995 widespread labeling of oligodendrocytes throughout the depth of motor cortex (M). Most labeled NHP
996 oligodendrocytes exhibit multipolar ramified morphology indicative of local axon myelination (N). Some
997 labeled oligodendrocytes exhibit morphologies suggesting wrapping around wider tubular structures
998 highlighted with dashed white lines (O). SYFP2-expressing cells of both morphological types express
999 the oligodendrocyte/OPC marker *SOX10* with high specificity (P).
- 1000 (Q-T) Prospective labeling of NHP astrocytes in vivo. eHGT_390m enhancer-AAV vector gives
1001 widespread labeling of astrocytes throughout the depth of somatosensory cortex (Q). A few large L5ET
1002 neurons are also labeled. Labeled astrocytes show the expected bushy morphology and GFAP
1003 immunoreactivity of astrocytes in parenchyma (R) and sometimes reside near walls of large-diameter
1004 tubular structures (S). SYFP2-expressing astrocytes express the astrocyte marker *FGFR3* with high
1005 specificity (T).

1006 Abbreviations: VISp primary visual cortex.

1007

1008



1009 **Figure 8: Astrocyte specific sensing of cholinergic signals in the nucleus accumbens during**
1010 **behavior.**

1011
1012 (A) 3xCore2(390m) driving expression of iAChSnFR. Enhancer vector is cloned into a pAAV plasmid
1013 and packaged into PHP.eB AAVs.

1014 (B) Coronal section showing stereotaxic injection of enhancer virus expressing iAChSnFR in the
1015 nucleus accumbens (injection coordinates: AP: 1.2, ML: 1.3, DV: 4.1).

1016 (C) Behavior and imaging experiment setup. Top: dynamic foraging behavior task schematic. Bottom:
1017 Fiber photometry instrumentation schematic and fiber location in a coronal section.

1018 (D) Fiber photometry signals of acetylcholine fluctuations during task performance. Top: ~30 min
1019 segment of a 2-hour session of dynamic foraging. Black dots represent the auditory cue, red dots
1020 represent time of first lick, blue dots represent water reward delivery. Bottom: 100 second (980-1080
1021 seconds) zoom in on above session with 6 individual trials (4 rewarded and 2 unrewarded trials).

1022 (E) Trial-averaged signals of rewarded and unrewarded trials aligned to time of first lick (mean \pm sem).

1023
1024

1025 **Extended Data Figure 1: Epigenetic characterization of candidate enhancers in additional**
1026 **chromatin accessibility datasets.**

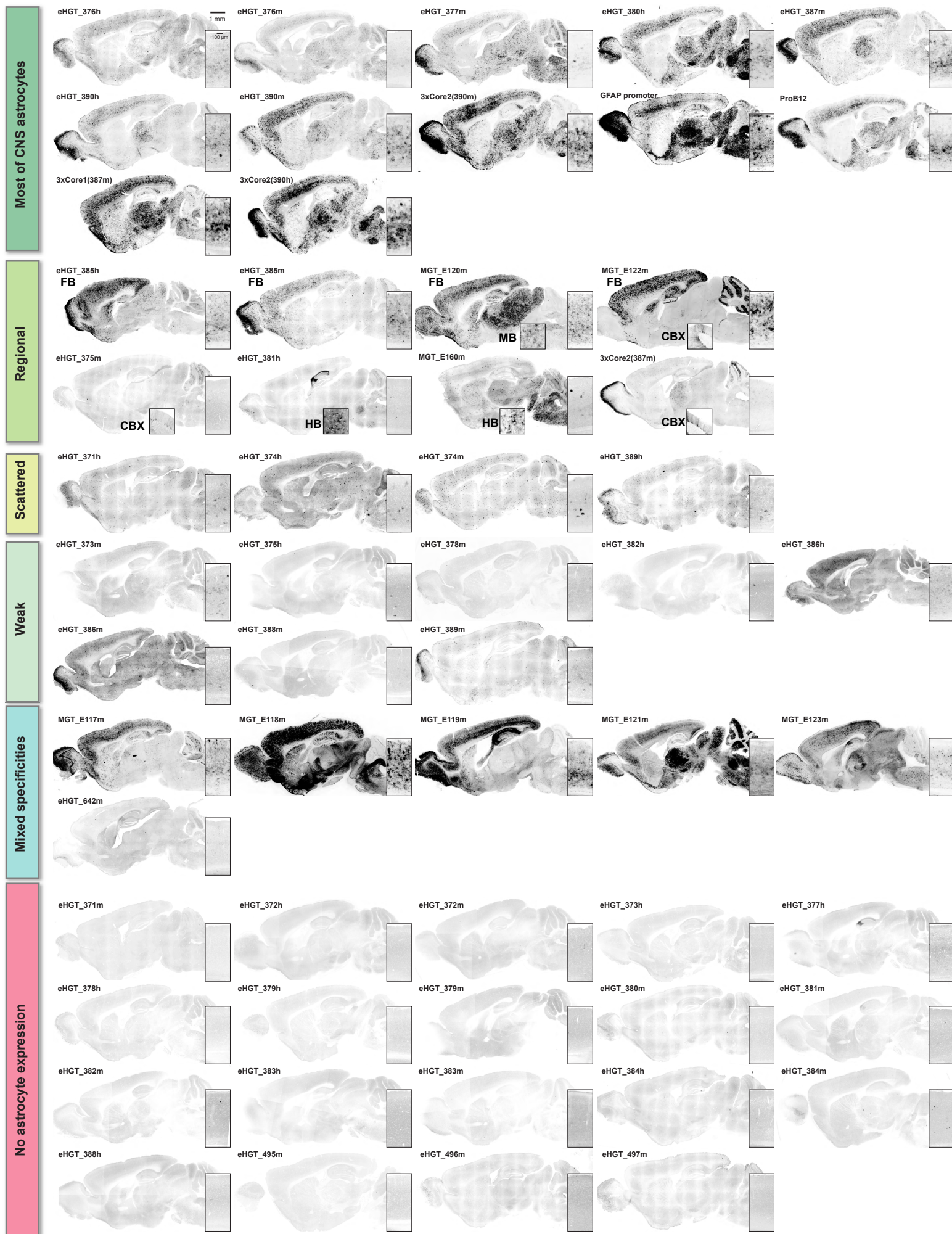
1027
1028 (A-D) Accessibility profiles of all tested candidate human astrocyte-specific (A,C) and human
1029 oligodendrocyte-specific (B, D) enhancers. Human enhancer regions are characterized in the datasets
1030 of Mich et al.³⁵ (A-B), who performed snATAC-seq on neurosurgical MTG samples, and of Fullard et
1031 al.⁸⁸ (C-D), who performed bulk ATAC-seq on neuronal (sorted NeuN⁺) and non-neuronal (sorted NeuN⁻
1032) nuclei from dissections spanning multiple regions of human postmortem forebrain. Overall, many
1033 candidate astrocyte- and oligodendrocyte-specific enhancers show accessibility specific to non-
1034 neuronal cells across much of the human forebrain.

1035 (E-F) Screening results from testing human candidate enhancers (same as Figure 1F-G, provided
1036 again for visualization). Testing result bar: Y = yes, enhancer-AAV gives strong or moderate on-target
1037 expression pattern; N = no, enhancer-AAV fails to express; W = weak on-target expression pattern; Mx
1038 = mixed specificities consisting of on-target cells plus unwanted neuronal populations; Off = off-target
1039 expression pattern, ND = no data.

1040 (G-H) Accessibility profiles for all tested candidate mouse astrocyte-specific (G) and oligodendrocyte-
1041 specific enhancers (H). Mouse enhancer regions are characterized in the dataset of Li et al.⁴⁸, who
1042 performed droplet-based snATAC-seq on many regions spanning the full mouse cerebrum.

1043 (I-J) Screening results from testing mouse candidate enhancers (same as Figure 1F-G, provided again
1044 for visualization).

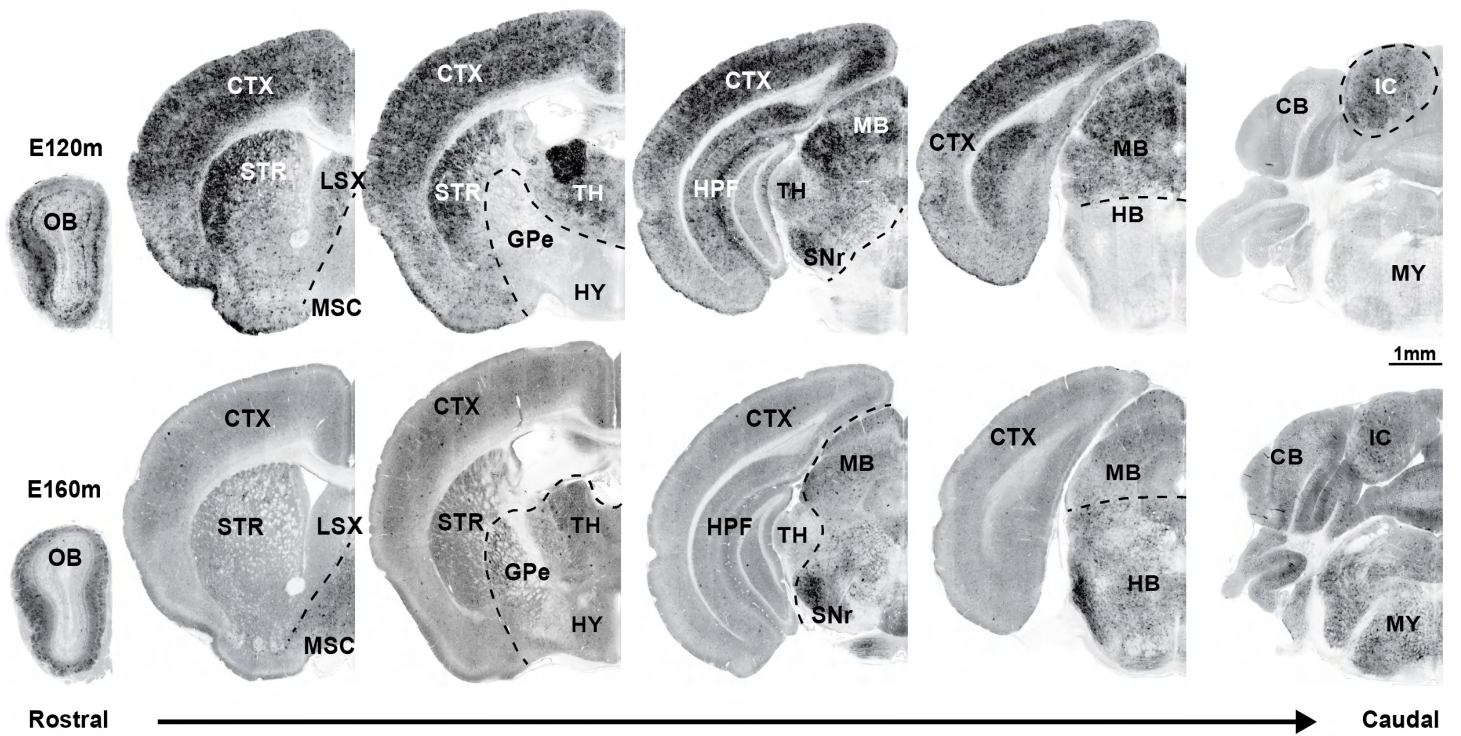
1045
1046



1047 **Extended Data Figure 2: Full screening results of all candidate enhancer-AAVs targeting**
1048 **astrocytes.**

1049 We injected mice with the indicated enhancer-AAV vectors between P42 and P56, then after 3-4 weeks
1050 we harvested brains, sliced them on a sliding microtome with freezing stage at 30 μ m thickness, co-
1051 stained the sections with DAPI, then mounted them with Vectashield Vybrance. Insets show a full
1052 cortical column from VISp (primary visual cortex), and in some cases also the labeling in MB (midbrain)
1053 or HB (hindbrain) or CBX (cerebellar cortex) is also shown. Astrocyte-specific enhancer-AAV vectors
1054 are broadly grouped by expression pattern into the following categories: “Most of CNS astrocytes”,
1055 “Regional” meaning present at medium-to-high levels in one or more broad brain regions but not all,
1056 “Scattered” meaning a few astrocytes are strongly labeled throughout the brain, “Weak” meaning many
1057 astrocytes throughout the brain are labeled at low level, “Mixed specificities” meaning one or more off-
1058 target neuron populations are also labeled in addition to astrocytes, and “No astrocyte expression”
1059 meaning failure to detect any clear astrocytes in these whole-brain sagittal images. These screening
1060 images were taken on multiple different microscopes, so the absolute levels of expression are difficult
1061 to compare directly across brains.

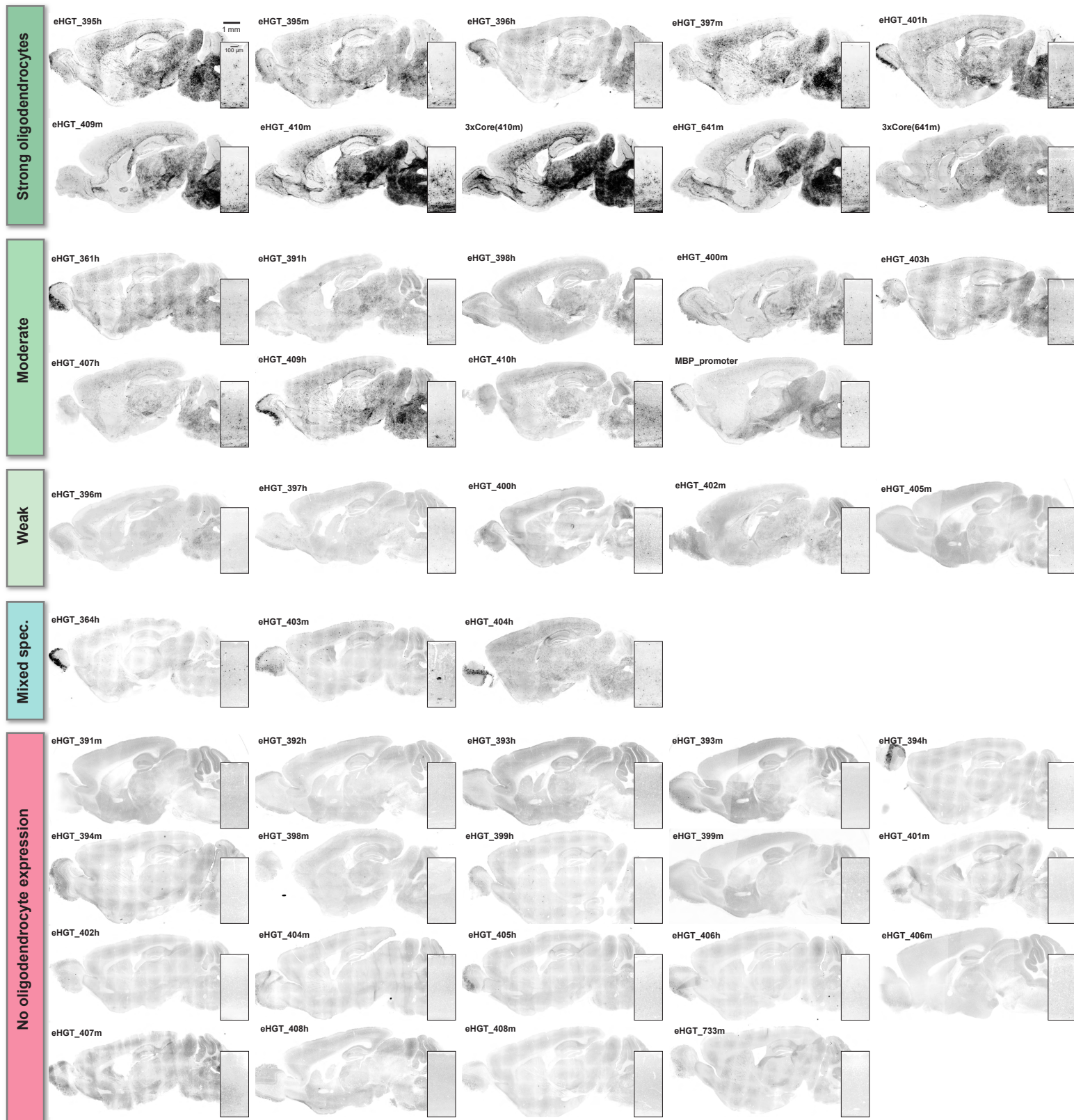
1062
1063



1064 **Extended Data Figure 3: Distinct astrocyte-specific expression domains of MGT_E120m and**
1065 **MGT_E160m.**

1066
1067 We injected mice with the indicated astrocyte-specific SYFP2-expressing enhancer-AAVs and
1068 performed whole-brain blockface imaging using the TissueCyte platform⁸². These vectors display
1069 largely non-overlapping zones of astrocyte expression: E120m is expressed in astrocytes within
1070 multiple forebrain structures including CTX, STR, OB, LSX, HPF, and TH, as well as MB, whereas
1071 E160m is expressed in MB, CBX, and HB structures as well as complementary forebrain structures
1072 including HY, MSC, and GPe, and OB. In the OB E120m is expressed in astrocytes within the granule
1073 cell layer, internal plexiform layer, and periglomerular cell layer, whereas E160m is expressed in a
1074 complementary pattern of astrocytes within the external plexiform layer.

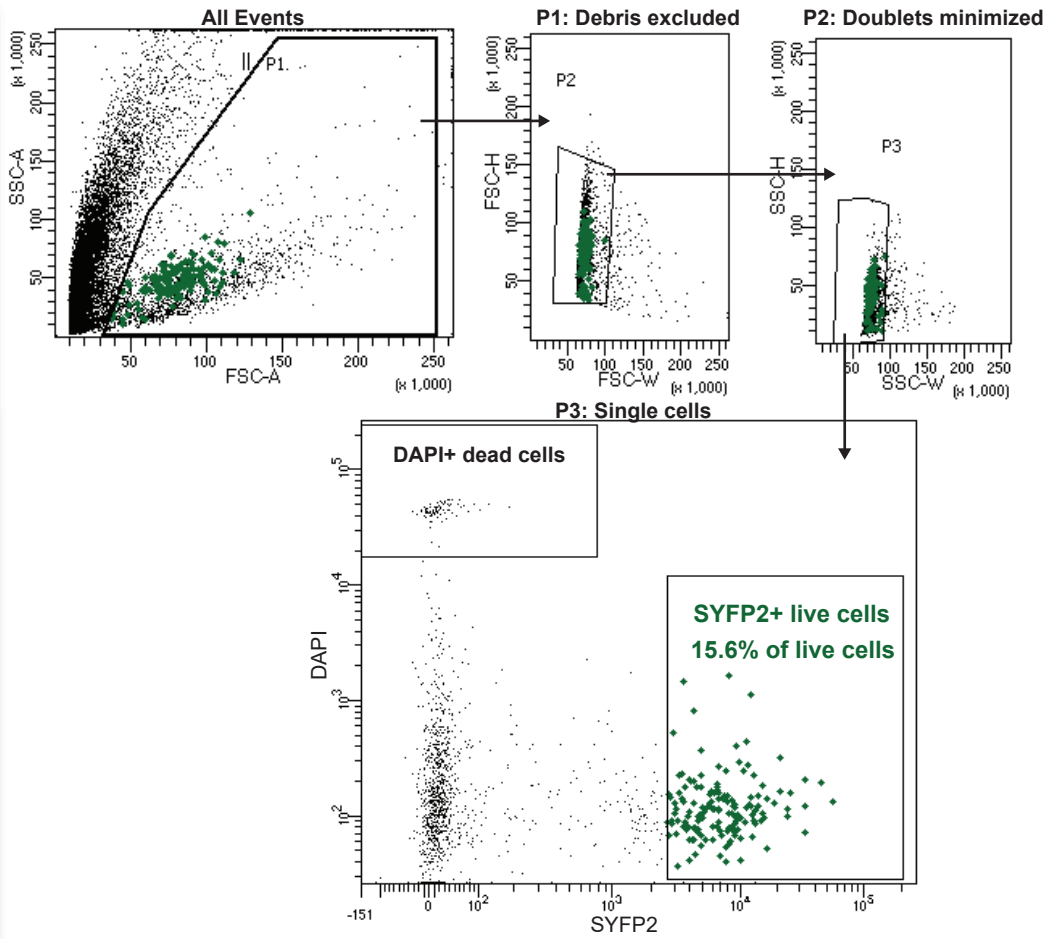
1075
1076 Abbreviations: CTX cerebral cortex, STR striatum, OB olfactory bulb, LSX lateral septal complex, HPF
1077 hippocampal formation, TH thalamus, MB midbrain, CBX cerebellar cortex, HB hindbrain, HY
1078 hypothalamus, MSC medial septal complex, GPe globus pallidus, external layer.
1079



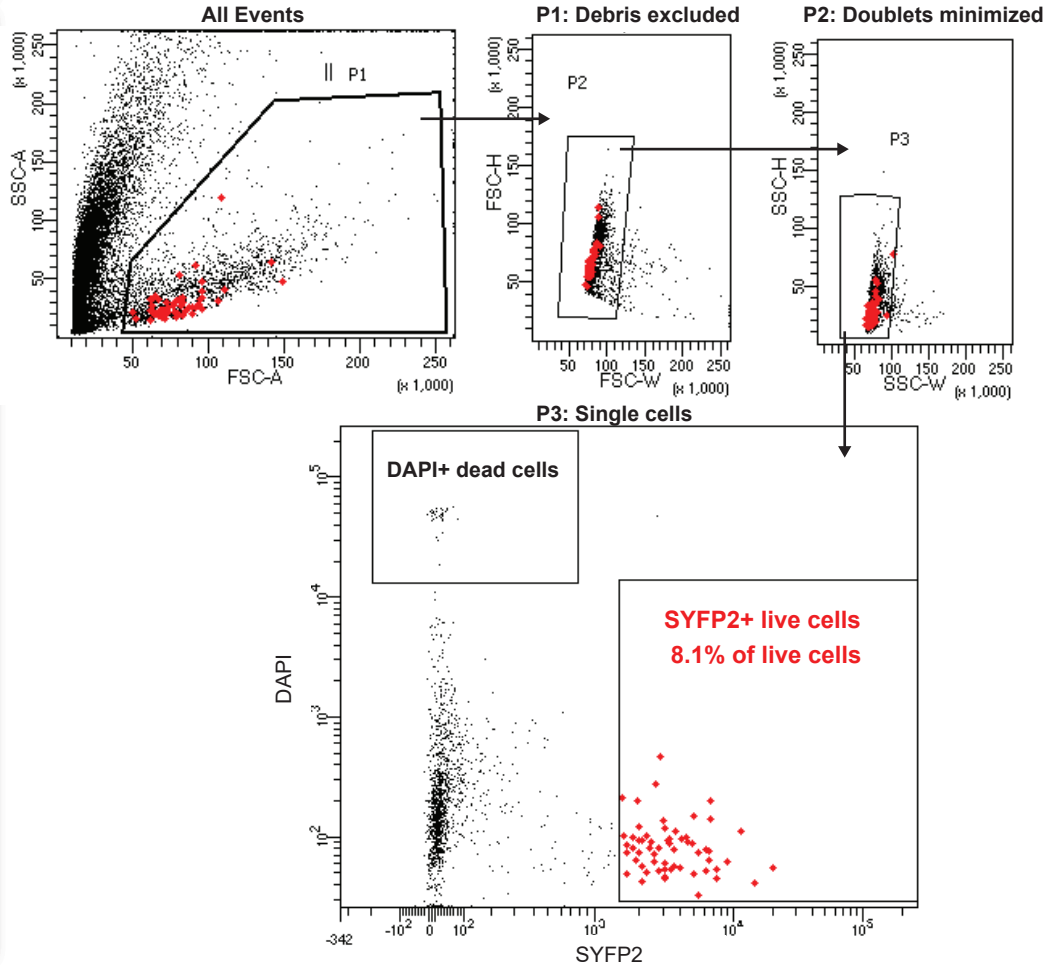
1080 **Extended Data Figure 4: Full screening results of all candidate enhancer-AAVs targeting**
1081 **oligodendrocytes.**

1082 We injected mice with the indicated enhancer-AAV vectors between P42 and P56, then after 3-4 weeks
1083 we harvested brains, sliced them on a sliding microtome with freezing stage at 30 μm thickness, co-
1084 stained the sections with DAPI, and mounted them with Vectashield Vybrance. Oligodendrocyte-
1085 specific enhancer-AAV vectors are broadly grouped by expression pattern into the following categories:
1086 “Strong oligodendrocytes”, “Weak” meaning many oligodendrocytes throughout the brain are labeled at
1087 low level, “Mixed specificities” meaning several off-target neuron or astrocyte populations are also
1088 present in addition to oligodendrocytes, and “No oligodendrocyte expression” meaning failure to detect
1089 any clear oligodendrocytes in these whole-brain sagittal images. These screening images were taken
1090 on multiple different microscopes, so the absolute levels of expression are difficult to compare directly
1091 across injections.
1092

3xCore2(390h) Astrocyte-specific



eHGT_396h Oligodendrocyte-specific



1093 **Extended Data Figure 5: Sorting enhancer-AAV-labeled astrocytes and oligodendrocytes.**

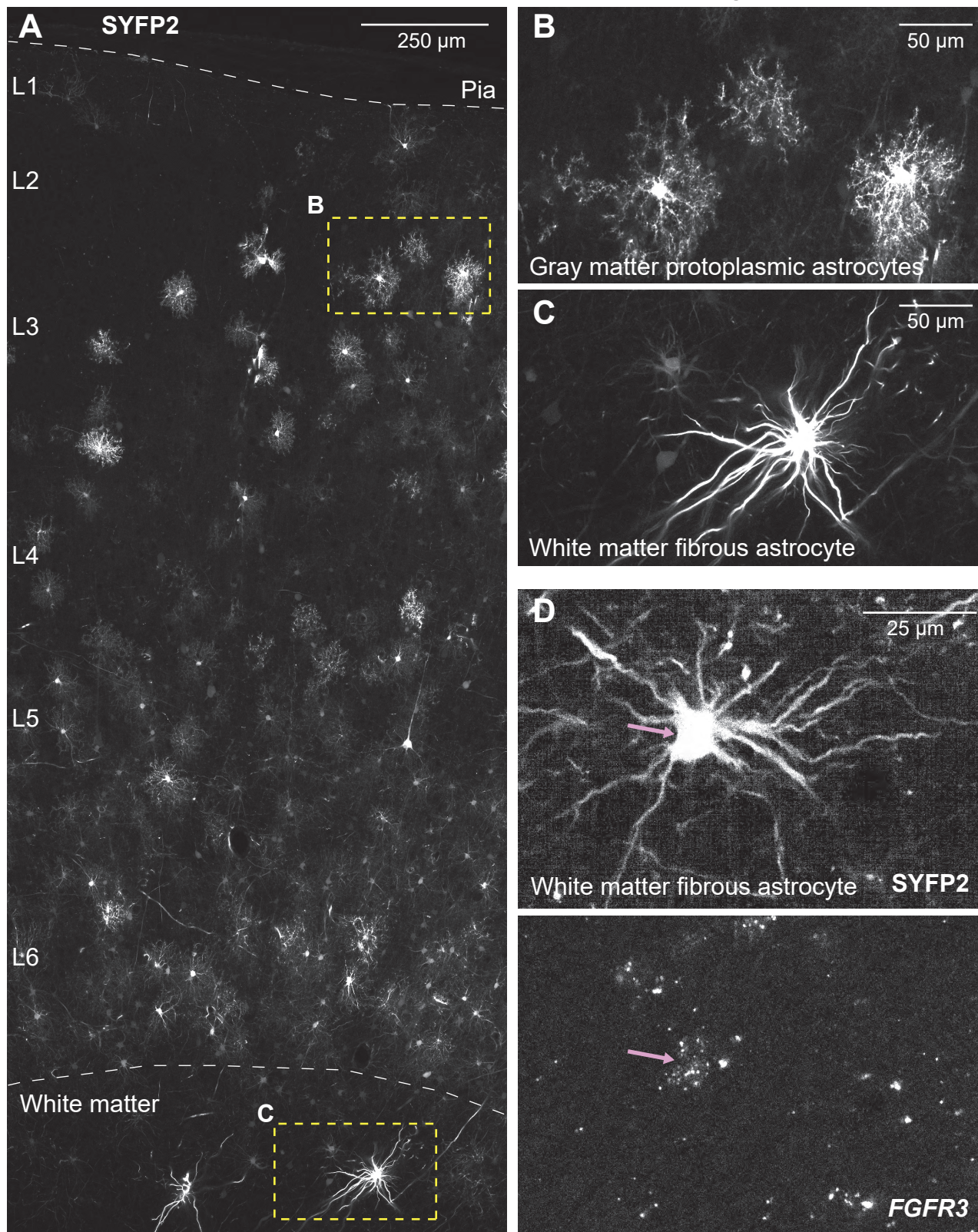
1094

1095 Example gating strategies for sorting 3xCore2(390h)-labeled astrocytes and eHGT_396h-labeled
1096 oligodendrocytes from mouse VISp.

1097

1098

eHGT_390m in NHP somatosensory cortex



1099 **Extended Data Figure 6: Diverse morphologies of NHP astrocytes labeled by enhancer-AAVs.**

1100

1101 (A-C) Labeling of both gray matter protoplasmic astrocytes and white matter fibrous astrocytes by
1102 eHGT_390m enhancer-AAV. We show full cortical column of a somatosensory cortex injection site in A,
1103 with expanded insets to show protoplasmic astrocytes in gray matter (B) and fibrous astrocytes in white
1104 matter (C).

1105 (D) Confirmation of astrocyte identity by mFISH. Fibrous astrocytes in white matter express the
1106 astrocyte marker *FGFR3*, similar to gray matter protoplasmic astrocytes (**Figure 7T**).

1107

Enhancer name	Identification scheme	Genome	Chr	Start	Stop	Enhancer_group	PhyloP	Length	Specificity	Strength (CPM)	Screen result	Expression pattern	Included in GLM model
eHGT_361h	Marker_gene	hg38	chrX	103780509	103781455	Human_Oligo	1.823	855	0.635	11.72	Yes	Oligodendrocytes_moderate	No
eHGT_361m	Marker_gene	mm10	chrX	136826512	136827460	Mouse_Oligo	1.488	807	0.879	12.03	No_data	No_data	No
eHGT_364h	Marker_gene	hg38	chr21	33051808	33052323	Human_Oligo	2.5	458	0.614	2.29	Mixed_spe	Mixed_specificity_oligodendrocy	No
eHGT_364m	Marker_gene	mm10	chr16	91246204	91246699	Mouse_Oligo	1.99	444	0.945	9.54	No_data	No_data	No
eHGT_371h	High_specificity	hg38	chr3	13485182	13485473	Human_Astro	0.967	269	0.454	3.81	Yes	Scattered_astrocytes	Yes
eHGT_371m	High_specificity	mm10	chr6	91160424	91160736	Mouse_Astro	0.87	241	0.216	4.28	No	No_astrocyte_expression	Yes
eHGT_372h	High_specificity	hg38	chr7	121914818	121915080	Human_Astro	0.33	216	0.668	2.6	No	No_astrocyte_expression	Yes
eHGT_372m	High_specificity	mm10	chr6	22910076	22910291	Mouse_Astro	0.194	187	0.742	2.85	No	No_astrocyte_expression	Yes
eHGT_373h	High_specificity	hg38	chr5	97134713	97135080	Human_Astro	0.537	329	0.72	3.81	No	No_astrocyte_expression	Yes
eHGT_373m	High_specificity	mm10	chr17	17409626	17409965	Mouse_Astro	0.531	319	0.909	11.78	Yes	Most_astrocytes_weak	Yes
eHGT_374h	High_specificity	hg38	chr15	64845370	64845672	Human_Astro	1.618	266	0.424	2.86	Yes	Scattered_astrocytes	Yes
eHGT_374m	High_specificity	mm10	chr9	65576810	65577101	Mouse_Astro	1.091	259	0.542	5.35	Yes	Scattered_astrocytes	Yes
eHGT_375h	High_specificity	hg38	chr13	99961720	99962046	Human_Astro	4.977	268	0.659	2.51	No	No_astrocyte_expression	Yes
eHGT_375m	High_specificity	mm10	chr14	122455334	122455655	Mouse_Astro	3.82	268	0.867	5.71	Yes	Bergmann_glia_astrocytes	Yes
eHGT_376h	High_specificity	hg38	chr3	188076136	188076690	Human_Astro	1.341	457	0.646	4.24	Yes	Most_astrocytes_strong	Yes
eHGT_376m	High_specificity	mm10	chr16	24326000	24326508	Mouse_Astro	1.083	435	0.865	11.78	Yes	Most_astrocytes_strong	Yes
eHGT_377h	High_specificity	hg38	chr10	80406003	80406485	Human_Astro	0.687	453	0.782	4.41	No	No_astrocyte_expression	Yes
eHGT_377m	High_specificity	mm10	chr14	41015471	41016233	Mouse_Astro	0.541	747	0.656	7.85	Yes	Most_astrocytes_strong	Yes
eHGT_378h	High_specificity	hg38	chr11	120182373	120182964	Human_Astro	2.312	559	0.681	6.32	No	No_astrocyte_expression	No
eHGT_378m	High_specificity	mm10	chr9	43268975	43269581	Mouse_Astro	1.699	559	0.911	12.49	Weak	Most_astrocytes_weak	No
eHGT_379h	High_specificity	hg38	chr3	64837170	64837760	Human_Astro	0.151	496	0.659	4.93	No	No_astrocyte_expression	Yes
eHGT_379m	High_specificity	mm10	chr6	93093752	93094309	Mouse_Astro	0.216	460	0.939	8.21	No	No_astrocyte_expression	Yes
eHGT_380h	High_specificity	hg38	chr6	44045566	44046145	Human_Astro	0.591	527	0.633	10.82	Yes	Most_astrocytes_strong	Yes
eHGT_380m	High_specificity	mm10	chr17	45765782	45766284	Mouse_Astro	0.536	479	0.727	7.14	No	No_astrocyte_expression	Yes
eHGT_381h	High_specificity	hg38	chr7	131400918	131401149	Human_Astro	2.166	173	0.4	1.9	Weak	Mid/hindbrain_astrocytes	No
eHGT_381m	High_specificity	mm10	chr6	31434638	31434879	Mouse_Astro	1.8	172	0.927	5.35	No	No_astrocyte_expression	No
eHGT_382h	High_specificity	hg38	chr10	113047655	113048169	Human_Astro	0.544	435	0.685	3.98	No	No_astrocyte_expression	Yes
eHGT_382m	High_specificity	mm10	chr19	55825471	55825949	Mouse_Astro	0.439	424	0.694	5.71	No	No_astrocyte_expression	Yes
eHGT_383h	High_specificity	hg38	chr2	220959419	220959789	Human_Astro	1.026	312	0.858	3.38	No	No_astrocyte_expression	Yes
eHGT_383m	High_specificity	mm10	chr1	76942759	76943103	Mouse_Astro	0.81	315	0.902	11.42	No	No_astrocyte_expression	Yes
eHGT_384h	High_specificity	hg38	chr6	121897357	121897797	Human_Astro	1.695	351	0.342	2.77	No	No_astrocyte_expression	Yes
eHGT_384m	High_specificity	mm10	chr10	56893293	56893720	Mouse_Astro	1.576	366	0.846	9.64	No	No_astrocyte_expression	Yes
eHGT_385h	High_specificity	hg38	chr9	123741938	123742543	Human_Astro	6.233	563	0.655	7.88	Weak	Telencephalon_astrocytes	No
eHGT_385m	High_specificity	mm10	chr2	38111566	38112219	Mouse_Astro	4.798	572	0.714	14.27	Yes	Telencephalon_astrocytes	No
eHGT_386h	High_specificity	hg38	chr1	15736012	15736372	Human_Astro	0.595	287	0.417	2.51	Weak	Most_astrocytes_weak	No
eHGT_386m	High_specificity	mm10	chr4	141623748	141624075	Mouse_Astro	1.042	231	0.527	5	Yes	Most_astrocytes_weak	No
eHGT_387h	High_specificity	hg38	chr1	219881964	219882484	Human_Astro	0.601	467	0.729	6.06	No_data	No_data	No
eHGT_387m	High_specificity	mm10	chr1	185493675	185494167	Mouse_Astro	0.633	425	0.959	15.35	Yes	Most_astrocytes_strong	No
eHGT_388h	High_specificity	hg38	chr12	20657459	20657845	Human_Astro	2.912	369	0.754	3.98	No	No_astrocyte_expression	Yes
eHGT_388m	High_specificity	mm10	chr6	141495577	141496010	Mouse_Astro	2.283	362	0.879	16.77	No	No_astrocyte_expression	Yes
eHGT_389h	High_specificity	hg38	chr20	63252174	63252906	Human_Astro	0.003	694	0.648	9.52	Yes	Scattered_astrocytes	No
eHGT_389m	High_specificity	mm10	chr2	180952658	180953361	Mouse_Astro	0.351	667	0.695	8.56	Weak	Most_astrocytes_weak	No
eHGT_390h	High_specificity	hg38	chr7	42152720	42153410	Human_Astro	7.463	634	0.699	8.91	Yes	Most_astrocytes_strong	Yes
eHGT_390m	High_specificity	mm10	chr13	15543638	15544333	Mouse_Astro	5.544	639	0.869	16.42	Yes	Most_astrocytes_strong	Yes
eHGT_391h	High_specificity	hg38	chr11	729607	730042	Human_Oligo	-0.132	419	0.688	7.49	Weak	Oligodendrocytes_moderate	No
eHGT_391m	High_specificity	mm10	chr7	141365022	141365541	Mouse_Oligo	0.135	474	0.901	13.2	No	No_oligodendrocyte_expression	No
eHGT_392h	High_specificity	hg38	chr4	48787039	48787541	Human_Oligo	1.369	431	0.776	6.88	No	No_oligodendrocyte_expression	No
eHGT_392m	High_specificity	mm10	chr5	73264044	73264568	Mouse_Oligo	1.225	448	0.832	4.25	No_data	No_data	No
eHGT_393h	High_specificity	hg38	chr18	66603993	66604511	Human_Oligo	2.036	451	0.755	7.23	No	No_oligodendrocyte_expression	Yes
eHGT_393m	High_specificity	mm10	chr1	110977271	110977865	Mouse_Oligo	1.391	548	0.593	6.16	No	No_oligodendrocyte_expression	Yes
eHGT_394h	High_specificity	hg38	chr3	171776470	171776980	Human_Oligo	0.518	444	0.782	5.2	No	No_oligodendrocyte_expression	Yes
eHGT_394m	High_specificity	mm10	chr3	27977667	27978413	Mouse_Oligo	0.254	661	0.738	12.62	No	No_oligodendrocyte_expression	Yes
eHGT_395h	High_specificity	hg38	chr9	128374105	128374728	Human_Oligo	2.782	595	0.742	9.96	Yes	Oligodendrocytes_strong	Yes
eHGT_395m	High_specificity	mm10	chr2	29830874	29831537	Mouse_Oligo	2.002	632	0.881	24.5	Yes	Oligodendrocytes_strong	Yes
eHGT_396h	High_specificity	hg38	chr11	117295457	117295798	Human_Oligo	1.384	302	0.561	3.88	Yes	Oligodendrocytes_strong	No

eHGT_396m	High_specificity	mm10	chr9	45854220	45854539	Mouse_Oligo	1.185	288	0.824	7.33	Weak	Oligodendrocytes_weak	No
eHGT_397h	High_specificity	hg38	chr15	44188767	44189188	Human_Oligo	1.986	396	0.591	4.67	Weak	Oligodendrocytes_weak	No
eHGT_397m	High_specificity	mm10	chr2	121799010	121799455	Mouse_Oligo	1.661	385	0.759	6.16	Yes	Oligodendrocytes_strong	No
eHGT_398h	High_specificity	hg38	chr16	57270420	57270919	Human_Oligo	1.042	475	0.793	7.49	Yes	Oligodendrocytes_moderate	Yes
eHGT_398m	High_specificity	mm10	chr8	94684265	94684766	Mouse_Oligo	1.199	446	0.806	11.74	No	No_oligodendrocyte_expression	Yes
eHGT_399h	High_specificity	hg38	chr2	36902653	36902934	Human_Oligo	4.206	253	0.628	2.73	No	No_oligodendrocyte_expression	Yes
eHGT_399m	High_specificity	mm10	chr17	78684296	78684576	Mouse_Oligo	3.818	249	0.885	4.11	No	No_oligodendrocyte_expression	Yes
eHGT_400h	High_specificity	hg38	chr4	114636222	114636638	Human_Oligo	2.948	372	0.605	3.88	Weak	Oligodendrocytes_weak	No
eHGT_400m	High_specificity	mm10	chr3	125898885	125899302	Mouse_Oligo	2.414	373	0.819	7.63	Yes	Oligodendrocytes_moderate	No
eHGT_401h	High_specificity	hg38	chr1	44592226	44592529	Human_Oligo	1.081	256	0.55	3.17	Yes	Oligodendrocytes_strong	Yes
eHGT_401m	High_specificity	mm10	chr4	117326998	117327312	Mouse_Oligo	1.024	271	0.778	3.96	No	No_oligodendrocyte_expression	Yes
eHGT_402h	High_specificity	hg38	chr17	75697915	75698299	Human_Oligo	0.976	320	0.626	4.67	No	No_oligodendrocyte_expression	No
eHGT_402m	High_specificity	mm10	chr11	115956504	115956883	Mouse_Oligo	0.956	326	0.919	13.94	Weak	Oligodendrocytes_weak	No
eHGT_403h	High_specificity	hg38	chr11	67410338	67410731	Human_Oligo	0.524	382	0.588	4.5	Yes	Oligodendrocytes_moderate	No
eHGT_403m	High_specificity	mm10	chr19	4183762	4184154	Mouse_Oligo	1.019	346	0.586	8.51	Mixed_spe	Mixed_specificity_oligodendrocyte	No
eHGT_404h	High_specificity	hg38	chr2	163943542	163943945	Human_Oligo	1.738	370	0.721	5.2	Mixed_spe	Mixed_specificity_oligodendrocyte	No
eHGT_404m	High_specificity	mm10	chr2	64325556	64326248	Mouse_Oligo	1.562	599	0.933	12.18	No	No_oligodendrocyte_expression	No
eHGT_405h	High_specificity	hg38	chr3	185175495	185175886	Human_Oligo	0.607	362	0.49	4.05	No	No_oligodendrocyte_expression	No
eHGT_405m	High_specificity	mm10	chr16	21724337	21724697	Mouse_Oligo	0.444	335	0.91	8.36	Weak	Oligodendrocytes_weak	No
eHGT_406h	High_specificity	hg38	chr2	88735239	88735593	Human_Oligo	-0.058	304	0.518	3.26	No	No_oligodendrocyte_expression	Yes
eHGT_406m	High_specificity	mm10	chr6	70774375	70774694	Mouse_Oligo	0.091	256	0.696	5.87	No	No_oligodendrocyte_expression	Yes
eHGT_407h	High_specificity	hg38	chr6	46098744	46099007	Human_Oligo	0.581	253	0.614	2.47	Yes	Oligodendrocytes_moderate	Yes
eHGT_407m	High_specificity	mm10	chr17	44121834	44122162	Mouse_Oligo	0.545	271	0.847	7.48	No	No_oligodendrocyte_expression	Yes
eHGT_408h	High_specificity	hg38	chr8	60867028	60867631	Human_Oligo	3.002	574	0.53	6.61	No	No_oligodendrocyte_expression	Yes
eHGT_408m	High_specificity	mm10	chr4	8867749	8868420	Mouse_Oligo	2.361	596	0.769	11.88	No	No_oligodendrocyte_expression	Yes
eHGT_409h	High_specificity	hg38	chr14	67539037	67539541	Human_Oligo	2.042	452	0.564	4.5	Yes	Oligodendrocytes_moderate	Yes
eHGT_409m	High_specificity	mm10	chr12	79035271	79035759	Mouse_Oligo	1.603	437	0.908	13.5	Yes	Oligodendrocytes_strong	Yes
eHGT_410h	High_specificity	hg38	chr9	81717541	81717791	Human_Oligo	2.177	202	0.579	1.41	Yes	Oligodendrocytes_moderate	Yes
eHGT_410m	High_specificity	mm10	chr4	72233773	72234067	Mouse_Oligo	1.838	203	0.817	9.68	Yes	Oligodendrocytes_strong	Yes
eHGT_495h	Marker_gene	hg38	chr19	33217923	33218346	Human_Astro	1.481	364	0.302	0.95	No_data	No_data	No
eHGT_495m	Marker_gene	mm10	chr7	35192340	35192802	Mouse_Astro	0.977	396	0.818	7.85	No	No_astrocyte_expression	No
eHGT_496h	Marker_gene	hg38	chr19	33225554	33226354	Human_Astro	1.18	749	0.516	4.76	No_data	No_data	No
eHGT_496m	Marker_gene	mm10	chr7	35185913	35186648	Mouse_Astro	0.955	686	0.734	15.35	No_data	No_data	No
eHGT_497h	Marker_gene	hg38	chr3	55237236	55237718	Human_Astro	1.648	437	0.037	0.09	No_data	No_data	No
eHGT_497m	Marker_gene	mm10	chr14	28781601	28782057	Mouse_Astro	1.444	410	0.966	7.49	No	No_astrocyte_expression	No
eHGT_641h	Marker_gene	hg38	chr21	33116993	33117641	Human_Oligo	4.073	557	0.755	16.66	No_data	No_data	No
eHGT_641m	Marker_gene	mm10	chr16	91305334	91305956	Mouse_Oligo	3.233	529	0.92	23.32	Yes	Oligodendrocytes_strong	No
eHGT_642h	Marker_gene	hg38	chr17	44539855	44540164	Human_Astro	2.026	230	0.463	0.26	No_data	No_data	No
eHGT_642m	Marker_gene	mm10	chr11	102579463	102579768	Mouse_Astro	1.655	228	0.86	11.06	Mixed_spe	Non-specific_astrocytes	No
eHGT_733m	Marker_gene	mm10	chr2	29273794	29274249	Mouse_Oligo	0.127	366	0.876	5.72	No	No_oligodendrocyte_expression	No
MGT_E117h	High_strength	hg38	chr7	23230417	23231661	Human_Astro	1.333	1213	0.197	4.15	No_data	No_data	No
MGT_E117m	High_strength	mm10	chr6	49020855	49022070	Mouse_Astro	1.202	1174	0.852	49.25	Mixed_spe	Non-specific_astrocytes	No
MGT_E118h	High_strength	hg38	chr13	25910516	25911691	Human_Astro	3.328	1146	0.062	0.26	No_data	No_data	No
MGT_E118m	High_strength	mm10	chr14	59736768	59737951	Mouse_Astro	2.384	1143	0.889	47.11	Mixed_spe	Mixed_specificity_astrocytes	No
MGT_E119h	High_strength	hg38	chr18	59386813	59388237	Human_Astro	4.406	1421	0.532	6.58	No_data	No_data	No
MGT_E119m	High_strength	mm10	chr18	66022617	66024006	Mouse_Astro	3.435	1386	0.926	38.9	Mixed_spe	Mixed_specificity_astrocytes	No
MGT_E120h	High_strength	hg38	chr2	134072857	134074292	Human_Astro	0.875	1436	0.333	2.16	No_data	No_data	No
MGT_E120m	High_strength	mm10	chr1	127159651	127161393	Mouse_Astro	0.697	1661	0.896	37.83	Yes	Forebrain_midbrain_astrocytes	No
MGT_E121h	High_strength	hg38	chr17	68641683	68642415	Human_Astro	0.531	733	0.139	0.17	No_data	No_data	No
MGT_E121m	High_strength	mm10	chr11	109753663	109754656	Mouse_Astro	0.322	994	0.911	38.9	Mixed_spe	Mixed_specificity_astrocytes	No
MGT_E122h	High_strength	hg38	chr4	175988170	175989315	Human_Astro	1.134	1121	0.675	8.65	No_data	No_data	No
MGT_E122m	High_strength	mm10	chr8	54791804	54792949	Mouse_Astro	1.078	1117	0.922	37.47	Yes	Forebrain_cerebellum_astrocyte	No
MGT_E123h	High_strength	hg38	chr14	80206581	80208078	Human_Astro	2.747	1497	0.701	12.12	No_data	No_data	No
MGT_E123m	High_strength	mm10	chr12	90733627	90735117	Mouse_Astro	2.427	1490	0.808	36.76	Mixed_spe	Mixed_specificity_astrocytes	No
MGT_E160h	None	hg38	chr2	48184996	48185538	Human_Astro	0.314	538	0	0	No_data	No_data	No
MGT_E160m	None	mm10	chr17	88297369	88297914	Mouse_Astro	0.347	516	0.282	1.07	Yes	Mid/hindbrain_astrocytes	No

1111 **Extended Data Table 1: Genomic coordinates, sequence characterization, and mouse screening**
1112 **results of all tested astrocyte and oligodendrocyte enhancers.**

1113 Calculations of parameters are as described in Methods section.

1114

1115 References

- 1116 1. Khakh, B. S. & Sofroniew, M. V. Diversity of astrocyte functions and phenotypes in neural
1117 circuits. *Nat. Neurosci.* **18**, 942–952 (2015).
- 1118 2. Zuchero, J. B. & Barres, B. A. Glia in mammalian development and disease. *Dev. Camb. Engl.*
1119 **142**, 3805–3809 (2015).
- 1120 3. Volkenhoff, A. *et al.* Glial Glycolysis Is Essential for Neuronal Survival in Drosophila. *Cell Metab.*
1121 **22**, 437–447 (2015).
- 1122 4. García-Cáceres, C. *et al.* Astrocytic Insulin Signaling Couples Brain Glucose Uptake with
1123 Nutrient Availability. *Cell* **166**, 867–880 (2016).
- 1124 5. Molofsky, A. V. *et al.* Astrocyte-encoded positional cues maintain sensorimotor circuit integrity.
1125 *Nature* **509**, 189–194 (2014).
- 1126 6. Liou, D. T. *et al.* A role for glia in the progression of Rett’s syndrome. *Nature* **475**, 497–500
1127 (2011).
- 1128 7. Wang, X. *et al.* Astrocytic Ca²⁺ signaling evoked by sensory stimulation in vivo. *Nat. Neurosci.* **9**,
1129 816–823 (2006).
- 1130 8. Sabelström, H. *et al.* Resident Neural Stem Cells Restrict Tissue Damage and Neuronal Loss
1131 After Spinal Cord Injury in Mice. *Science* **342**, 637–640 (2013).
- 1132 9. Liddelow, S. A. *et al.* Neurotoxic reactive astrocytes are induced by activated microglia. *Nature*
1133 **541**, 481–487 (2017).
- 1134 10. Hasel, P., Rose, I. V. L., Sadick, J. S., Kim, R. D. & Liddelow, S. A. Neuroinflammatory astrocyte
1135 subtypes in the mouse brain. *Nat. Neurosci.* **24**, 1475–1487 (2021).
- 1136 11. Zuchero, J. B. *et al.* CNS Myelin Wrapping Is Driven by Actin Disassembly. *Dev. Cell* **34**, 152–
1137 167 (2015).
- 1138 12. Steadman, P. E. *et al.* Disruption of Oligodendrogenesis Impairs Memory Consolidation in Adult
1139 Mice. *Neuron* **105**, 150-164.e6 (2020).
- 1140 13. Wilkins, A., Majed, H., Layfield, R., Compston, A. & Chandran, S. Oligodendrocytes Promote
1141 Neuronal Survival and Axonal Length by Distinct Intracellular Mechanisms: A Novel Role for
1142 Oligodendrocyte-Derived Glial Cell Line-Derived Neurotrophic Factor. *J. Neurosci.* **23**, 4967–
1143 4974 (2003).
- 1144 14. Knowles, J. K. *et al.* Maladaptive myelination promotes generalized epilepsy progression. *Nat.*
1145 *Neurosci.* **25**, 596–606 (2022).
- 1146 15. Zhang, P. *et al.* Senolytic therapy alleviates A β -associated oligodendrocyte progenitor cell
1147 senescence and cognitive deficits in an Alzheimer’s disease model. *Nat. Neurosci.* **1** (2019)
1148 doi:10.1038/s41593-019-0372-9.
- 1149 16. La Manno, G. *et al.* Molecular architecture of the developing mouse brain. *Nature* **596**, 92–96
1150 (2021).
- 1151 17. Yao, Z. *et al.* A taxonomy of transcriptomic cell types across the isocortex and hippocampal
1152 formation. *Cell* **184**, 3222-3241.e26 (2021).
- 1153 18. Boisvert, M. M., Erikson, G. A., Shokhirev, M. N. & Allen, N. J. The Aging Astrocyte
1154 Transcriptome from Multiple Regions of the Mouse Brain. *Cell Rep.* **22**, 269–285 (2018).
- 1155 19. Endo, F. *et al.* Molecular basis of astrocyte diversity and morphology across the CNS in health
1156 and disease. *Science* **378**, eadc9020 (2022).
- 1157 20. Yao, Z. *et al.* A high-resolution transcriptomic and spatial atlas of cell types in the whole mouse
1158 brain. 2023.03.06.531121 Preprint at <https://doi.org/10.1101/2023.03.06.531121> (2023).
- 1159 21. Hodge, R. D. *et al.* Conserved cell types with divergent features in human versus mouse cortex.
1160 *Nature* **573**, 61–68 (2019).
- 1161 22. Chen, Z.-P. *et al.* Lipid-accumulated reactive astrocytes promote disease progression in
1162 epilepsy. *Nat. Neurosci.* **26**, 542–554 (2023).

- 1163 23. Wang, C. *et al.* Selective removal of astrocytic APOE4 strongly protects against tau-mediated
1164 neurodegeneration and decreases synaptic phagocytosis by microglia. *Neuron* (2021)
1165 doi:10.1016/j.neuron.2021.03.024.
- 1166 24. Monje, M. *et al.* Hedgehog-responsive candidate cell of origin for diffuse intrinsic pontine glioma.
1167 *Proc. Natl. Acad. Sci. U. S. A.* **108**, 4453–4458 (2011).
- 1168 25. Alcantara Llaguno, S. *et al.* Malignant Astrocytomas Originate from Neural Stem/Progenitor Cells
1169 in a Somatic Tumor Suppressor Mouse Model. *Cancer Cell* **15**, 45–56 (2009).
- 1170 26. Deverman, B. E. *et al.* Cre-dependent selection yields AAV variants for widespread gene transfer
1171 to the adult brain. *Nat. Biotechnol.* **34**, 204–209 (2016).
- 1172 27. Chan, K. Y. *et al.* Engineered AAVs for efficient noninvasive gene delivery to the central and
1173 peripheral nervous systems. *Nat. Neurosci.* **20**, 1172–1179 (2017).
- 1174 28. Nonnenmacher, M. *et al.* Rapid evolution of blood-brain-barrier-penetrating AAV capsids by
1175 RNA-driven biopanning. *Mol. Ther. - Methods Clin. Dev.* **20**, 366–378 (2021).
- 1176 29. De, A., El-Shamayleh, Y. & Horwitz, G. D. Fast and reversible neural inactivation in macaque
1177 cortex by optogenetic stimulation of GABAergic neurons. *eLife* **9**, e52658 (2020).
- 1178 30. El-Shamayleh, Y., Kojima, Y., Soetedjo, R. & Horwitz, G. D. Selective Optogenetic Control of
1179 Purkinje Cells in Monkey Cerebellum. *Neuron* **95**, 51-62.e4 (2017).
- 1180 31. Mendell, J. R. *et al.* Single-Dose Gene-Replacement Therapy for Spinal Muscular Atrophy.
1181 <http://dx.doi.org/10.1056/NEJMoa1706198>
1182 [https://www.nejm.org/doi/10.1056/NEJMoa1706198?url_ver=Z39.88-](https://www.nejm.org/doi/10.1056/NEJMoa1706198?url_ver=Z39.88-2003&rfr_id=ori%3Arid%3Acrossref.org&rfr_dat=cr_pub%3Dwww.ncbi.nlm.nih.gov)
1183 [2003&rfr_id=ori%3Arid%3Acrossref.org&rfr_dat=cr_pub%3Dwww.ncbi.nlm.nih.gov](https://www.ncbi.nlm.nih.gov) (2017)
1184 doi:10.1056/NEJMoa1706198.
- 1185 32. Dimidschstein, J. *et al.* A viral strategy for targeting and manipulating interneurons across
1186 vertebrate species. *Nat. Neurosci.* **19**, 1743–1749 (2016).
- 1187 33. Vormstein-Schneider, D. *et al.* Viral manipulation of functionally distinct interneurons in mice,
1188 non-human primates and humans. *Nat. Neurosci.* 1–8 (2020) doi:10.1038/s41593-020-0692-9.
- 1189 34. Hrvatin, S. *et al.* A scalable platform for the development of cell-type-specific viral drivers. *eLife*
1190 **8**, e48089 (2019).
- 1191 35. Mich, J. K. *et al.* Functional enhancer elements drive subclass-selective expression from mouse
1192 to primate neocortex. *Cell Rep.* **34**, 108754 (2021).
- 1193 36. Graybuck, L. T. *et al.* Enhancer viruses for combinatorial cell-subclass-specific labeling. *Neuron*
1194 **109**, 1449-1464.e13 (2021).
- 1195 37. Jüttner, J. *et al.* Targeting neuronal and glial cell types with synthetic promoter AAVs in mice,
1196 non-human primates and humans. *Nat. Neurosci.* **22**, 1345–1356 (2019).
- 1197 38. Lin, C.-H. *et al.* Identification of cis-regulatory modules for adeno-associated virus-based cell-
1198 type-specific targeting in the retina and brain. *J. Biol. Chem.* **298**, (2022).
- 1199 39. Wang, L.-L. *et al.* Revisiting astrocyte to neuron conversion with lineage tracing in vivo. *Cell* **184**,
1200 5465-5481.e16 (2021).
- 1201 40. Xie, Y., Zhou, J. & Chen, B. Critical examination of Ptbp1-mediated glia-to-neuron conversion in
1202 the mouse retina. *Cell Rep.* **39**, 110960 (2022).
- 1203 41. Le, N., Appel, H., Pannullo, N., Hoang, T. & Blackshaw, S. Ectopic insert-dependent neuronal
1204 expression of GFAP promoter-driven AAV constructs in adult mouse retina. *Front. Cell Dev. Biol.*
1205 **10**, (2022).
- 1206 42. Borden, P. M. *et al.* A fast genetically encoded fluorescent sensor for faithful in vivo acetylcholine
1207 detection in mice, fish, worms and flies. 2020.02.07.939504 Preprint at
1208 <https://doi.org/10.1101/2020.02.07.939504> (2020).
- 1209 43. Fröhlich, D. *et al.* Dual-function AAV gene therapy reverses late-stage Canavan disease
1210 pathology in mice. *Front. Mol. Neurosci.* **15**, 1061257 (2022).
- 1211 44. Hillen, A. E. J. *et al.* In vivo targeting of a variant causing vanishing white matter using
1212 CRISPR/Cas9. *Mol. Ther. - Methods Clin. Dev.* **25**, 17–25 (2022).

- 1213 45. Hagemann, T. L. *et al.* Antisense therapy in a rat model of Alexander disease reverses GFAP
1214 pathology, white matter deficits, and motor impairment. *Sci. Transl. Med.* **13**, eabg4711 (2021).
1215 46. Lister, R. *et al.* Global Epigenomic Reconfiguration During Mammalian Brain Development.
1216 *Science* **341**, 1237905 (2013).
1217 47. Luo, C. *et al.* Single-cell methylomes identify neuronal subtypes and regulatory elements in
1218 mammalian cortex. *Science* **357**, 600–604 (2017).
1219 48. Lee, D.-S. *et al.* Simultaneous profiling of 3D genome structure and DNA methylation in single
1220 human cells. *Nat. Methods* **16**, 999–1006 (2019).
1221 49. Liu, H. *et al.* DNA methylation atlas of the mouse brain at single-cell resolution. *Nature* **598**, 120–
1222 128 (2021).
1223 50. Fullard, J. F. *et al.* Open chromatin profiling of human postmortem brain infers functional roles for
1224 non-coding schizophrenia loci. *Hum. Mol. Genet.* (2019) doi:10.1093/hmg/ddy229.
1225 51. Li, Y. E. *et al.* An atlas of gene regulatory elements in adult mouse cerebrum. *Nature* **598**, 129–
1226 136 (2021).
1227 52. Lee, Y., Messing, A., Su, M. & Brenner, M. GFAP promoter elements required for region-specific
1228 and astrocyte-specific expression. *Glia* **56**, 481–493 (2008).
1229 53. Sun, W. *et al.* SOX9 Is an Astrocyte-Specific Nuclear Marker in the Adult Brain Outside the
1230 Neurogenic Regions. *J. Neurosci.* **37**, 4493–4507 (2017).
1231 54. Gow, A., Friedrich, V. L., Jr & Lazzarini, R. A. Myelin basic protein gene contains separate
1232 enhancers for oligodendrocyte and Schwann cell expression. *J. Cell Biol.* **119**, 605–616 (1992).
1233 55. Bin, J. M., Harris, S. N. & Kennedy, T. E. The oligodendrocyte-specific antibody ‘CC1’ binds
1234 Quaking 7. *J. Neurochem.* **139**, 181–186 (2016).
1235 56. Bailey, T. L. *et al.* MEME Suite: tools for motif discovery and searching. *Nucleic Acids Res.* **37**,
1236 W202–W208 (2009).
1237 57. Hume, M. A., Barrera, L. A., Gisselbrecht, S. S. & Bulyk, M. L. UniPROBE, update 2015: new
1238 tools and content for the online database of protein-binding microarray data on protein–DNA
1239 interactions. *Nucleic Acids Res.* **43**, D117–D122 (2015).
1240 58. Kulakovskiy, I. V. *et al.* HOCOMOCO: towards a complete collection of transcription factor
1241 binding models for human and mouse via large-scale ChIP-Seq analysis. *Nucleic Acids Res.* **46**,
1242 D252–D259 (2018).
1243 59. Castro-Mondragon, J. A. *et al.* JASPAR 2022: the 9th release of the open-access database of
1244 transcription factor binding profiles. *Nucleic Acids Res.* **50**, D165 (2022).
1245 60. Furushima, K., Murata, T., Kiyonari, H. & Aizawa, S. Characterization of Opr deficiency in mouse
1246 brain: Subtle defects in dorsomedial telencephalon and medioventral forebrain. *Dev. Dyn.* **232**,
1247 1056–1061 (2005).
1248 61. Inoue, T., Ota, M., Ogawa, M., Mikoshiba, K. & Aruga, J. Zic1 and Zic3 Regulate Medial
1249 Forebrain Development through Expansion of Neuronal Progenitors. *J. Neurosci.* **27**, 5461–5473
1250 (2007).
1251 62. Hornig, J. *et al.* The Transcription Factors Sox10 and Myrf Define an Essential Regulatory
1252 Network Module in Differentiating Oligodendrocytes. *PLOS Genet.* **9**, e1003907 (2013).
1253 63. Turnescu, T. *et al.* Sox8 and Sox10 jointly maintain myelin gene expression in oligodendrocytes.
1254 *Glia* **66**, 279–294 (2018).
1255 64. Hinderer, C. *et al.* Severe Toxicity in Nonhuman Primates and Piglets Following High-Dose
1256 Intravenous Administration of an Adeno-Associated Virus Vector Expressing Human SMN. *Hum.*
1257 *Gene Ther.* **29**, 285–298 (2018).
1258 65. Zhang, K. *et al.* A cell atlas of chromatin accessibility across 25 adult human tissues.
1259 2021.02.17.431699 <https://www.biorxiv.org/content/10.1101/2021.02.17.431699v1> (2021)
1260 doi:10.1101/2021.02.17.431699.
1261 66. Goertsen, D. *et al.* AAV capsid variants with brain-wide transgene expression and decreased
1262 liver targeting after intravenous delivery in mouse and marmoset. *Nat. Neurosci.* **25**, 106–115
1263 (2022).

- 1264 67. Martín-Suárez, S., Abiega, O., Ricobaraza, A., Hernandez-Alcoceba, R. & Encinas, J. M.
1265 Alterations of the Hippocampal Neurogenic Niche in a Mouse Model of Dravet Syndrome. *Front.*
1266 *Cell Dev. Biol.* **8**, (2020).
- 1267 68. Madisen, L. *et al.* A robust and high-throughput Cre reporting and characterization system for the
1268 whole mouse brain. *Nat. Neurosci.* **13**, 133–140 (2010).
- 1269 69. Hartung, M. & Kisters-Woike, B. Cre Mutants with Altered DNA Binding Properties*. *J. Biol.*
1270 *Chem.* **273**, 22884–22891 (1998).
- 1271 70. Sayeg, M. K. *et al.* Rationally Designed MicroRNA-Based Genetic Classifiers Target Specific
1272 Neurons in the Brain. *ACS Synth. Biol.* **4**, 788–795 (2015).
- 1273 71. Cho, F. S. *et al.* Enhancing GAT-3 in thalamic astrocytes promotes resilience to brain injury in
1274 rodents. *Sci. Transl. Med.* **14**, eabj4310 (2022).
- 1275 72. Hasel, P., Aisenberg, W. H., Bennett, F. C. & Liddelow, S. A. Molecular and metabolic
1276 heterogeneity of astrocytes and microglia. *Cell Metab.* **35**, 555–570 (2023).
- 1277 73. Aida, T. *et al.* Astroglial glutamate transporter deficiency increases synaptic excitability and leads
1278 to pathological repetitive behaviors in mice. *Neuropsychopharmacol. Off. Publ. Am. Coll.*
1279 *Neuropsychopharmacol.* **40**, 1569–1579 (2015).
- 1280 74. Li, Z. *et al.* Cell-Type-Specific Afferent Innervation of the Nucleus Accumbens Core and Shell.
1281 *Front. Neuroanat.* **12**, (2018).
- 1282 75. Beier, K. T. *et al.* Circuit Architecture of VTA Dopamine Neurons Revealed by Systematic Input-
1283 Output Mapping. *Cell* **162**, 622–634 (2015).
- 1284 76. Ren, J. *et al.* Anatomically Defined and Functionally Distinct Dorsal Raphe Serotonin Sub-
1285 systems. *Cell* **175**, 472-487.e20 (2018).
- 1286 77. Ren, J. *et al.* Single-cell transcriptomes and whole-brain projections of serotonin neurons in the
1287 mouse dorsal and median raphe nuclei. *eLife* **8**, e49424 (2019).
- 1288 78. Gabitto, M. I. *et al.* Integrated multimodal cell atlas of Alzheimer’s disease. 2023.05.08.539485
1289 Preprint at <https://doi.org/10.1101/2023.05.08.539485> (2023).
- 1290 79. Kamath, T. *et al.* Single-cell genomic profiling of human dopamine neurons identifies a
1291 population that selectively degenerates in Parkinson’s disease. *Nat. Neurosci.* **25**, 588–595
1292 (2022).
- 1293 80. Pagès, Hervé. BSgenome: Software infrastructure for efficient representation of full genomes
1294 and their SNPs. R package version 1.62.0. (2021).
- 1295 81. Kim, J.-Y., Grunke, S. D., Levites, Y., Golde, T. E. & Jankowsky, J. L. Intracerebroventricular
1296 Viral Injection of the Neonatal Mouse Brain for Persistent and Widespread Neuronal
1297 Transduction. *JoVE J. Vis. Exp.* e51863 (2014) doi:10.3791/51863.
- 1298 82. Ragan, T. *et al.* Serial two-photon tomography for automated ex vivo mouse brain imaging. *Nat.*
1299 *Methods* **9**, 255–258 (2012).
- 1300 83. Tasic, B. *et al.* Shared and distinct transcriptomic cell types across neocortical areas. *Nature*
1301 **563**, 72 (2018).
- 1302 84. Traag, V. A., Waltman, L. & van Eck, N. J. From Louvain to Leiden: guaranteeing well-connected
1303 communities. *Sci. Rep.* **9**, 5233 (2019).
- 1304 85. Choi, J.-H. *et al.* Optimization of AAV expression cassettes to improve packaging capacity and
1305 transgene expression in neurons. *Mol. Brain* **7**, 17 (2014).
- 1306 86. Bari, B. A. *et al.* Stable Representations of Decision Variables for Flexible Behavior. *Neuron* **103**,
1307 922-933.e7 (2019).
- 1308 87. Akam, T. & Walton, M. E. pyPhotometry: Open source Python based hardware and software for
1309 fiber photometry data acquisition. *Sci. Rep.* **9**, 3521 (2019).
- 1310 88. Fullard, J. F. *et al.* An atlas of chromatin accessibility in the adult human brain. *Genome Res.* **28**,
1311 1243–1252 (2018).
- 1312